LIDA: the Leiden ice database for astrochemistry

Rocha, W.R.M.; Rachid, M.G.; Olsthoorn, B.; Dishoeck, E.F. van; McClure, M.K.; Linnartz, H.

Astronomy & Astrophysics

LIDA: The Leiden Ice Database for Astrochemistry

W. R. M. Rocha[1,3] ⓘ, M. G. Rachid[1] ⓘ, B. Olsthoorn[2], E. F. van Dishoeck[3] ⓘ, M. K. McClure[3] ⓘ, and H. Linnartz[1] ⓘ

[1] Laboratory for Astrophysics, Leiden Observatory, Leiden University, PO Box 9513, 2300 RA Leiden, The Netherlands
e-mail: rocha@strw.leidenuniv.nl
[2] Nordita, KTH Royal Institute of Technology and Stockholm University, Hannes Alfvéns väg 12, 114 21 Stockholm, Sweden
[3] Leiden Observatory, Leiden University, PO Box 9513, 2300 RA Leiden, The Netherlands

ABSTRACT

Context. High-quality vibrational spectra of solid-phase molecules in ice mixtures and for temperatures of astrophysical relevance are needed to interpret infrared observations toward protostars and background stars. Such data are collected worldwide by several laboratory groups in support of existing and upcoming astronomical observations. Over the last 25 yr, the Laboratory for Astrophysics at Leiden Observatory has provided more than 1100 (high-resolution) spectra of diverse ice samples.

Aims. In time with the recent launch of the *James Webb* Space Telescope, we have fully upgraded the Leiden Ice Database for Astrochemistry (LIDA) adding recently measured spectra. The goal of this paper is to describe what options exist regarding accessing and working with a large collection of infrared (IR) spectra, and the ultraviolet–visible (UV/vis) to the mid-infrared refractive index of H_2O ice. This also includes astronomy-oriented online tools to support the interpretation of IR ice observations.

Methods. This ice database is based on open-source Python software, such as `Flask` and `Bokeh`, used to generate the web pages and graph visualization, respectively. Structured Query Language (SQL) is used for searching ice analogs within the database and `Jmol` allows for three-dimensional molecule visualization. The database provides the vibrational modes of molecules known and expected to exist as ice in space. These modes are characterized using density functional theory with the `ORCA` software. The IR data in the database are recorded via transmission spectroscopy of ice films condensed on cryogenic substrates. The real UV/vis refractive indices of H_2O ice are derived from interference fringes created from the simultaneous use of a monochromatic HeNe laser beam and a broadband Xe-arc lamp, whereas the real and imaginary mid-IR values are theoretically calculated. LIDA not only provides information on fundamental ice properties, but it also offers online tools. The first tool, SPECFY, is directly linked to the data in the database to create a synthetic spectrum of ices towards protostars. The second tool allows the uploading of external files and the calculation of mid-infrared refractive index values.

Results. LIDA provides an open-access and user-friendly platform to search, download, and visualize experimental data of astrophysically relevant molecules in the solid phase. It also provides the means to support astronomical observations; in particular, those that will be obtained with the *James Webb* Space Telescope. As an example, we analysed the Infrared Space Observatory spectrum of the protostar AFGL 989 using the resources available in LIDA and derived the column densities of H_2O, CO and CO_2 ices.

Key words. astrochemistry – solid state: volatile – astronomical databases: miscellaneous

1. Introduction

Infrared (IR) spectroscopy is a diagnostic tool used to characterize chemical structures of molecules and distinguish their functional groups (e.g., Coblentz 1905; Balkanski 1989). For this reason, a number of laboratories around the world have been focusing on providing laboratory-based IR data of interstellar ice analogs for a range of different ice compositions and temperatures (e.g., Hagen et al. 1979; Strazzulla et al. 1984; Schmitt et al. 1989; Grim et al. 1989; Hudgins et al. 1993; Boudin et al. 1998; Palumbo et al. 1998; Schutte 1999; Muñoz Caro et al. 2002; Öberg et al. 2009; Pilling et al. 2010; Vinogradoff et al. 2015; Terwisscha van Scheltinga et al. 2018, 2021; Urso et al. 2020; Rachid et al. 2020, 2021; Potapov et al. 2021). IR spectra directly represent the molecular geometry of a molecule and as such can act as a molecular fingerprint. In the gas phase and at very high resolution, such rovibrationally resolved spectra are unique; although, overlap may still occur. In the solid state, however, interactions with the ice matrix prohibit molecules from (freely) rotating and cause spectra to broaden and shift with respect to the unperturbed gas-phase value. Additionally, spectral overlaps are more

common. The amount of broadening and shifting depends on ice composition (both ice constituents and concentration) and ice temperature, as well as other parameters such as the level of ice porosity. In dedicated laboratory studies, all these parameters can be derived under fully controlled conditions. Examples can be found in Öberg et al. (2007).

IR spectroscopy is also the technique widely used to detect solid-phase molecules in the interstellar medium (ISM; e.g., Gillett & Forrest 1973; Schutte et al. 1996; Pontoppidan et al. 2003; Gibb et al. 2004; Boogert et al. 2008, 2013; Zasowski et al. 2009; Bottinelli et al. 2010; Penteado et al. 2015; Perotti et al. 2020; Rocha et al. 2021; Onaka et al. 2021). The light of a protostar, edge-on disk, or background star passes through the circumstellar material, and absorption features in the IR are seen in the protostellar spectral energy distribution (SED). The correct interpretation of those absorption bands is only possible upon comparison with the spectra of ice analogs measured in the laboratory. With this methodology, important discoveries have been made through observations of space- and ground-based telescopes such as the Infrared Space Observatory (ISO), the *Spitzer* Space Telescope/Infrared Spectrograph (IRS), and the Infrared Spectrometer And Array Camera mounted on the Very

Large Telescope (VLT/ISAAC). To date, the molecules securely identified in ices are H_2O, CO, CO_2, NH_3, CH_4, and CH_3OH (Öberg et al. 2011; Boogert et al. 2015), and the isotopologues are ^{13}CO and $^{13}CO_2$ (Boogert et al. 2002a). Except in the cases of CO and ^{13}CO, which have only one vibrational mode, these molecules were identified in astrophysical ices by the detection of multiple absorption bands across the IR spectrum. These identifications in ices allowed us to study the solid-phase chemistry in different astrophysical environments. For example, amorphous water ice is predominantly found toward background stars and low-mass protostars (Smith et al. 1989; Boogert et al. 2008), whereas a certain fraction of crystalline water ice was found in the circumstellar material of high-mass protostars (Dartois et al. 2002). CO is also an important discriminator of the ice environment, and astronomical observations indicate that it does not only exist in the pure form, but it can also be mixed with CO_2, H_2O, or CH_3OH (e.g., Pontoppidan et al. 2003; Cuppen et al. 2011). In the case of CO_2 ice, the bending mode around 15 μm provides a diagnostic of heating and segregation of polar and apolar molecules in ices (e.g., Ehrenfreund et al. 1996; Pontoppidan et al. 2008; Isokoski et al. 2013). Among the list of molecules identified in ices, CH_3OH (methanol) belongs to the group of so-called complex organic molecules (COMs), which, in astrochemistry, are defined as organic molecules containing six or more atoms (e.g., $C_xH_yY_z$, with Y = O, N, P, S; Herbst & van Dishoeck 2009). A number of small molecules have been tentatively identified in ices for which only one vibrational mode could be assigned from astronomical observations. This list also includes sulfur-bearing molecules (notably, SO_2; Boogert et al. 1997) and ions (notably OCN^-; Schutte & Greenberg 1997).

Many different COMs have been identified in the gas phase through radio and submillimeter surveys (e.g., Blake et al. 1987; Jørgensen et al. 2012, 2020; McGuire et al. 2016; Belloche et al. 2020; van Gelder et al. 2020; McGuire 2022; Nazari et al. 2021; Rivilla et al. 2021; Brunken et al. 2022), but astronomical observations have not been able to unambiguously identify frozen COMs larger than CH_3OH due to low spectral resolution or sensitivity. Nevertheless, tentative detections of CH_3CHO (acetaldehyde) and CH_3CH_2OH (ethanol) ice have been reported in the literature (Schutte et al. 1999; Öberg et al. 2011; Terwisscha van Scheltinga et al. 2018; Rocha & Pilling 2015; Rocha et al. 2021). Consistently with these tentative detections, several laboratory experiments have shown that such molecules can be formed in ices. Some examples are interstellar ice analogs processed by UV radiation (e.g., Bernstein et al. 1995; Muñoz Caro & Schutte 2003; Öberg et al. 2009; Meinert et al. 2016; Öberg 2016; Nuevo et al. 2018; Ishibashi et al. 2021; Bulak et al. 2021), electron bombardment (e.g., Brown et al. 1982; Materese et al. 2015; Mifsud et al. 2021), X-rays (e.g., Pilling & Bergantini 2015; Ciaravella et al. 2019), cosmic rays (e.g., Hudson et al. 2001; Domaracka et al. 2010; Pilling et al. 2010), and via thermal processing (e.g., Danger et al. 2011; Theulé et al. 2013). Other mechanisms excluding the presence of energetic triggers, such as atom addition reactions that are more representative of dark cloud conditions, have also been shown to result in the formation of COMs (Watanabe & Kouchi 2002; Fuchs et al. 2009; Theulé et al. 2013; Linnartz et al. 2015; Fedoseev et al. 2017; Ioppolo et al. 2021).

Apart from IR spectroscopy, the complex refractive index (CRI) of ice samples is important for the interpretation of astronomical observations. CRI is given by a complex number, $\tilde{m} = n + ik$, where n and k are the real and imaginary parts and are associated with scattering and absorption effects, respectively. In protostellar environments, CRI has been used to evaluate the

effect of icy grain sizes and shapes in the spectral features of ices (e.g., Ehrenfreund et al. 1997; Boogert et al. 2002b, 2008; Pontoppidan et al. 2005; Rocha & Pilling 2015; Perotti et al. 2020; Dartois et al. 2022). For example, Boogert et al. (2008) observed a dependence of the libration mode of H_2O ice peak position on the size of spherical grains. Better fits of this band are obtained when small grains are adopted in the models. Similarly, CRI values have been used to interpret the absorption band at 3 μm, which is associated with the O–H stretching mode of H_2O (e.g., Smith et al. 1989; Dartois & d'Hendecourt 2001). In the Solar System, the CRI also plays a crucial role in the simulation of reflected light due to icy surfaces to interpret spectral observations. (e.g., Clark et al. 2012; Dalle Ore et al. 2015). Finally, the CRI may be used to construct opacities for a dust grain size distribution model (Weingartner & Draine 2001), which can be used with a radiative transfer code to self-consistently calculate the temperature and density distributions of dusty astronomical objects, for example, protoplanetary disks (D'Alessio et al. 2006).

The advances in the identification of molecules in both the gas and solid phases have been strongly supported by atomic and molecular data in open-access databases. In fact, electronic databases have become an essential tool in the context of astrochemistry, given the large amount of data that are produced by laboratory experiments. In particular, the astrochemical community targeting gas-phase chemical species is well served with multiple databases. For example, the Cologne Database for Molecular Spectroscopy[1] (CDMS; Müller et al. 2001, 2005; Endres et al. 2016) and the Jet Propulsion Laboratory[2] (JPL; Pickett et al. 1998; Pearson et al. 2010) databases provide catalogs with transition frequencies, energy levels, and line strengths for atoms and molecules in the gas-phase of astrophysical and atmospheric interest. Collisional rate coefficients are available through the Leiden Atomic and Molecular Database (LAMDA)[3] for non-LTE excitation (Schöier et al. 2005; van der Tak et al. 2020). Similarly, BASECOL contains a repository of collisional ro-vibrational excitation data of molecules by colliding with different agents such as atoms, ions, molecules, or electrons (Dubernet et al. 2006, 2013). More oriented to chemical reactions, the UMIST Database for Astrochemistry[4] (UDfA; McElroy et al. 2013) contains the reaction rates of more than 6000 gas-phase reactions. In a similar vein, the Kinetic Database for Astrochemistry[5] (KIDA; Wakelam et al. 2012) has provided reaction rate coefficients for a massive number of chemical species for astrochemical studies. The photodissociation and photoionization values of gas-phase molecules relevant for astrophysics are available online[6] and described by Heays et al. (2017), van Dishoeck et al. (2006), and van Dishoeck (1988). The properties of gas-phase polycyclic aromatic hydrocarbons (PAHs) are widely available through the NASA Ames PAH IR Spectroscopy Database[7] (Bauschlicher et al. 2010; Boersma et al. 2014; Mattioda et al. 2020).

The astrochemistry community working with solid-phase materials has also been served with databases. The refractive index of refractory materials is available via the Database of

---

[1] https://cdms.astro.uni-koeln.de/
[2] https://spec.jpl.nasa.gov/
[3] https://home.strw.leidenuniv.nl/~moldata/
[4] http://udfa.ajmarkwick.net/
[5] https://kida.astrochem-tools.org/
[6] https://home.strw.leidenuniv.nl/~ewine/photo/index.html
[7] https://www.astrochemistry.org/pahdb/

Optical Constants for Cosmic Dust[8] (Henning et al. 1999; Jäger et al. 2003). Likewise, IR spectra of binary ice mixtures and refractive indexes of pure ices can be found on the web page of the Cosmic Ice Laboratory[9] from NASA (e.g., Moore et al. 2010; Knez et al. 2012; Gerakines & Hudson 2020) and at Databases of the Astrophysics & Astrochemistry Laboratory[10], which contains measurements by Hudgins et al. (1993). A database of refractive indices of ice samples irradiated by heavy ions is also available on the Laboratório de Astroquímica e Astrobiologia da Univap (LASA) webpage[11] with calculations performed by Rocha & Pilling (2014, 2018), and Rocha et al. (2020). Infrared refractive indices of CO and CO_2 ices are available from the Experimental Astrophysics Laboratory on the Catania Astrophysical Observatory website[12] (Baratta & Palumbo 1998). Finally, we also mention the Solid Spectroscopy Hosting Architecture of Databases and Expertise[13] (SSHADE; Schmitt et al. 2018), which contains a compilation of spectral and photometric data obtained by various spectroscopic techniques over the whole electromagnetic spectrum from gamma to radio wavelengths, through X-rays, UV, vis, IR, and millimeter ranges. The data are not limited to ices, but also contain measurements of liquids, minerals, rocks, and organic and carbonaceous materials.

Similarly to many of the databases mentioned above, the Leiden Database for Ices has served the astronomical community since the 1990s, but until recently no COM spectra were included, and the spectral resolution of the data was around 1–2 cm^{-1} (e.g., Gerakines et al. 1996; Ehrenfreund et al. 1996, 1997). Additionally, the data were fragmented into several databases targeting specific ice samples. To continue supporting the interpretation of ice observations with current and future telescopes, in particular the *James Webb* Space Telescope (JWST), we have fully upgraded the Leiden Ice Database for Astrochemistry (LIDA[14]). In particular, LIDA is a deliverable of the Early Release Science program ICE AGE[15] (PI: Melissa McClure; Co-PIs: Adwin Boogert, Harold Linnartz). In LIDA, all data are now available in one central location, and appealing features are included such as a search capability and dynamic data visualization. Additionally, online tools are included in LIDA to support JWST data analysis or to prepare observing blocks, by deriving integration times based on expected column densities. LIDA covers the most abundant solid-phase species observed in the ISM, which are listed in Table 1, along with information about their secure, tentative, or non-identification in the solid phase in astrophysical environments from previous observations. The JWST has the technical potential to enlarge the inventory of ice identifications in space, and several programs (ERS, Guaranteed Time Observations – GTO and General Observer - GO) will search for new ice features toward protostars and background stars using high spatial- and spectral-resolution observing modes. Moreover, the JWST will shed light on the mystery surrounding the formation of COMs in ices. For this purpose, comparison with spectra of COMs in astrophysically relevant ice matrices at high spectral resolution is needed.

Such data are required for a range of different physical conditions, such as mixing ratios, temperatures and porosity levels, as these differences affect the spectral appearance of the ice absorption bands.

This manuscript systematically guides (new) users through LIDA. Section 2 and the appendix give an overview of the data available in the 2022 version of LIDA and describe the type of data and how they were obtained. Section 3 provides information about the database structure, namely, the relational design, web interface, and visualization tools. In Sect. 4, we introduce the computational online tools dedicated to supporting JWST data analysis. An application illustrating the potential of LIDA is also shown. Section 5 points out the upgrades on LIDA that are intended for the coming years. A summary of this work is provided in Sect. 6.

2. Data in the database

In this section, we provide details on the experimental techniques used to measure the data available through LIDA. In summary, LIDA contains mid-infrared (mid-IR) spectra of ice samples ($\sim$4000–500 cm^{-1}; 2.5–20 μm) and ultraviolet–visible (UV/vis) to mid-IR refractive indices of water ice in the 0.25–20 μm range. The IR ice spectra are available for pure and mixed ices for different settings. The amorphous and crystalline H_2O ice refractive indices (*n* and *k*) are available for ices deposited at different temperatures.

2.1. Experimental setups and ice growth techniques

Between 1990 and 2020, the majority of the IR data in Leiden were recorded with our HV setup, a regular high vacuum setup (10^{-7} mbar) in which the broadband light of a Fourier Transform IR spectrometer (best resolution 0.1 cm^{-1}) is transmitted through a cryogenically cooled substrate covered with ice that is grown under fully controlled laboratory conditions (Fig. 1a). The transmitted beam is focused into a detector and processed with a Fourier transform to provide the transmitted light per wavelength. In the 1990s, this setup was also equipped with a microwave discharge hydrogen flow lamp that was used to irradiate ice samples with a flux of $\sim 10^{15}$ photons cm^{-2} s^{-1} dominated by Lyman-α emission in order to study radical or ionic ice constituents or species formed upon irradiation (Gerakines et al. 1996). The HV setup has been regularly upgraded and details are available in Öberg et al. (2009). A new setup has been used since 2020: infrared absorption setup for ice spectroscopy (IRASIS) uses the same measurement principle but operates at substantially lower pressures (10^{-9} mbar) to minimize contaminants. Moreover, laser interferometry has been incorporated to perform thickness measurements in order to derive experimental absorption cross-sections. All these data are recorded in transmission. Details concerning IRASIS are available in Rachid et al. (2021). In the near future, a quartz crystal micro-balance will also be incorporated. A few spectra available from LIDA have been recorded using reflection absorption IR (RAIRS) spectroscopy (Fig. 1b), but they are not included in the collection of ice spectra presented in this paper. The reader can find more details about those experiments in van Broekhuizen (2005), Fuchs et al. (2006), Öberg et al. (2009), Fayolle et al. (2011) and Ligterink et al. (2018); moreover, the CRYOgenic Photoproduct Analysis Device (CRYOPAD) is a setup that uses RAIRS and is dedicated to study the impact of vacuum UV irradiation on ice samples.

Apart from ice spectra, we also present real UV/vis refractive index measurements at cryogenic temperatures using

---

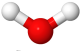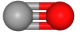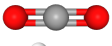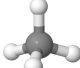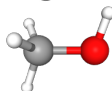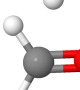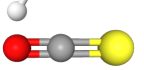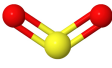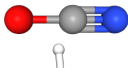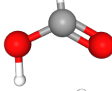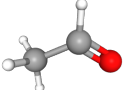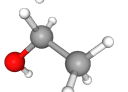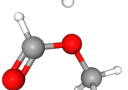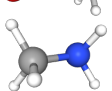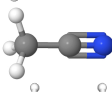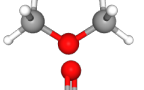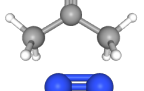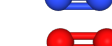**Table 1.** List of molecules with relevant data on LIDA and their solid-phase (tentative or non-) detection in the ISM.

Chemical structure [a]	Chemical formula	Name	Notes on LIDA				Solid-phase [b,c] detection/Ref.
			IR spectrum	UV/vis-mid IR	Heating	UV irr.	
	H_2O	Water	Yes	Yes	Yes	Yes	✓ / [1]
	CO	Carbon monoxide	Yes	No	Yes	Yes	✓ / [2]
	CO_2	Carbon dioxide	Yes	No	Yes	Yes	✓ / [3]
	CH_4	Methane	Yes	No	Yes	Yes	✓ / [4]
	NH_3	Ammonia	Yes	No	Yes	Yes	✓ / [5]
	CH_3OH	Methanol	Yes	No	Yes	Yes	✓ / [6]
	NH_4^+	Ammonium ion	Yes	No	No	No	⚠ / [7]
	H_2CO	Formaldehyde	Yes	No	No	No	⚠ / [8]
	OCS	Carbonyl sulfide	Yes	No	Yes	No	⚠ / [9]
	SO_2	Sulfur dioxide	Yes	No	No	No	⚠ / [10]
	OCN^-	Cyanate ion	Yes	No	No	No	⚠ / [11]
	HCOOH	Formic acid	Yes	No	Yes	No	⚠ / [7]
	CH_3CHO	Acetaldehyde	Yes	No	Yes	No	⚠ / [12]
	CH_3CH_2OH	Ethanol	Yes	No	Yes	No	⚠ / [13]
	CH_3OCHO	Methyl formate	Yes	No	Yes	No	⚠ / [14]
	CH_3NH_2	Methylamine	Yes	No	Yes	No	⚠ / [15]
	CH_3CN	Acetonitrile	Yes	No	Yes	No	⚠ / [16]
	CH_3OCH_3	Dimethyl ether	Yes	No	Yes	No	✗ / ...
	CH_3COCH_3	Acetone	Yes	No	Yes	No	✗ / ...
	N_2	Nitrogen	Yes	No	Yes	No	✗ / ...
	O_2	Oxygen	Yes	No	Yes	No	✗ / ...

Notes. [a] Taken from https://pubchem.ncbi.nlm.nih.gov/. [b] Symbols for detection – ✓: secure; ⚠: tentative; ✗: no. [c] All these molecules have also been detected in the gas-phase, except the ions NH_4^+ and OCN^- (see 2021 census in McGuire 2022).

References. [1] Gillett & Forrest (1973), [2] Lacy et al. (1984), [3] de Graauw et al. (1996), [4] Lacy et al. (1991), [5] Lacy et al. (1998), [6] Grim et al. (1989), [7] Schutte et al. (1996), [8] Keane et al. (2001), [9] Palumbo et al. (1995), [10] Boogert et al. (1997), [11] Schutte & Greenberg (1997), [12] Schutte et al. (1999), [13] Öberg et al. (2011), [14] Terwisscha van Scheltinga et al. (2018), [15] Rachid et al. (2021), [16] Rachid et al. (2022).
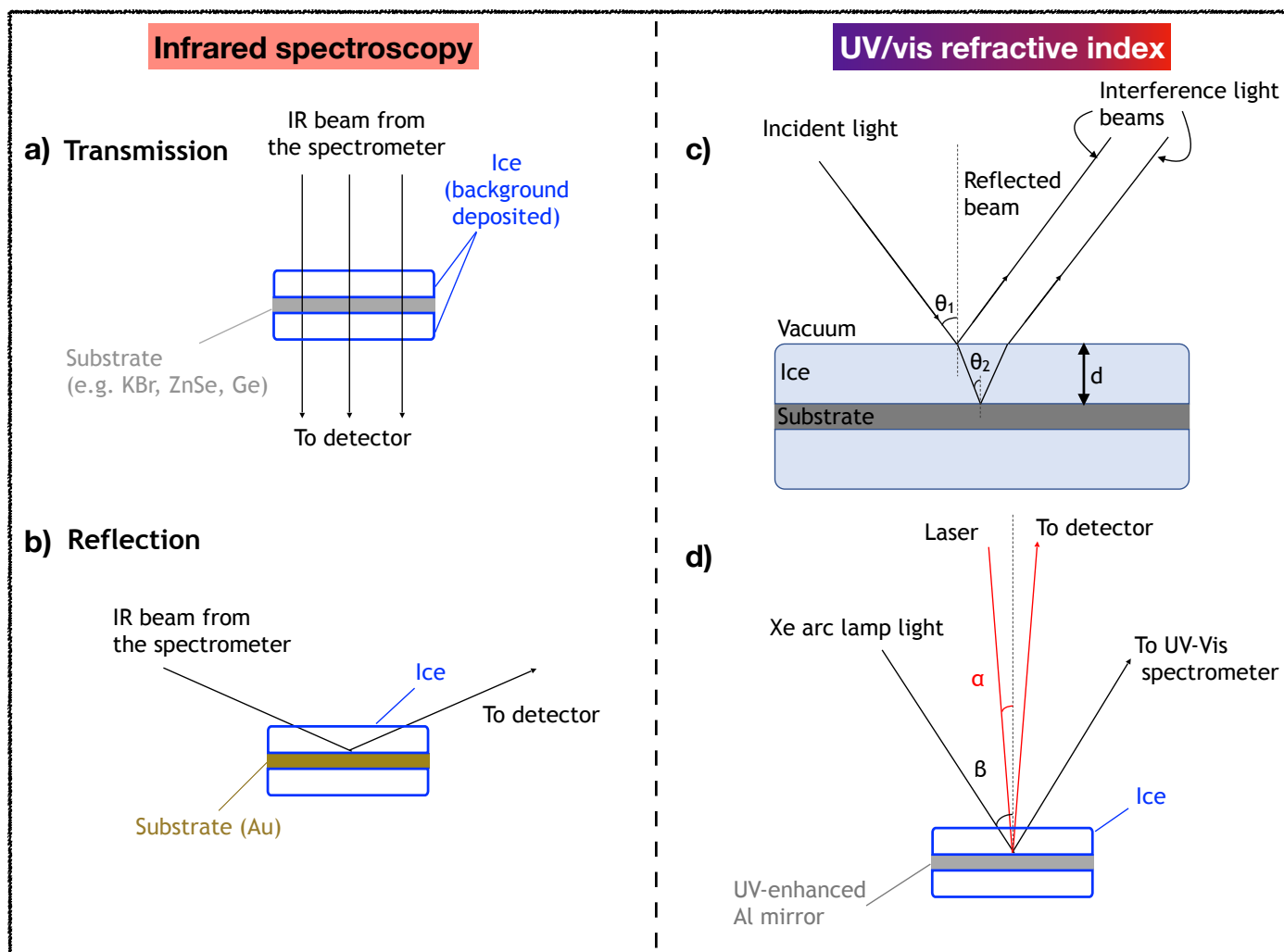
Fig. 1. Overview of experimental techniques used to obtain data hosted in LIDA. The *left panel* shows two infrared spectroscopic techniques used to record the spectrum of ices; namely, transmission mode (*a*) and reflection-absorption mode (*b*). The *right panel* illustrates the technique used to measure UV/vis refractive index values. Cartoon *c* provides details of the diffraction and reflection phenomena that generate an interference pattern during ice growth. Cartoon *d* shows the incidence and reflection of the monochromatic and broadband light beams when interacting with the ice.

our optical absorption setup for ice spectroscopy (OASIS; Kofman et al. 2019; He et al. 2022). The base pressure on OASIS is around 6×10^{-8} mbar. In this setup, a light source impinges on the growing ice and the reflected beam creates an interference pattern (Fig. 1c). Specifically, an Xe arc lamp and an HeNe laser (632 nm) are the light sources for the interference technique (Fig. 1d). The light from the Xe arc lamp strikes the growing ice at 45 degrees and is reflected toward the aperture of an Andor 303i Shamrock spectrometer. In the spectrometer, the light is dispersed and collected on a charge-coupled device (CCD; Andor iDus DV420 OE), which allows us to record the interference pattern at different wavelengths in the 250 and 750 nm region. The HeNe beam strikes the ice at a low angle ($\sim3°$) and is recorded by a photodetector. The interference pattern is later used to derive the refractive index of the ice (see Sect. 2.3). So far, the OASIS experiments have targeted measurements of pure ices. In the near future, this setup will be used to measure the refractive index of binary ice mixtures as well.

In IRASIS, OASIS, and CRYOPAD, a single gas/vapour component or a gaseous mixture is introduced into the chamber through a controllable leak valve and deposited onto a cold substrate. Usually, the substrate used in transmission spectroscopy is one of the following materials: potassium bromide – KBr, zinc selenide – ZnSe, or germanium – Ge; whereas, gold (Au) is used for RAIRS. A UV-enhanced aluminium mirror is used as a substrate in refractive index experiments. In most of the data available from LIDA, the ices are background-deposited, which means that the gas inlet does not point toward the sample, allowing the molecules to impinge onto the substrate coming from random directions and to adhere to both sides of it. This is more representative of the way molecules interact with an icy dust grain in space and generally causes the ice to be somewhat more porous. In the case of mixed ices, the samples can be prepared in a separate mixing system or by admitting the individual gas/vapor components in the chamber through different dosing lines. In either case, the molecules are considered to be homogeneously mixed before freezing out onto the cooled substrate. The ice thickness is often given as the number of monolayers or as Langmuir, where one monolayer (1L) corresponds to 10^{15} cm^{-2} (Langmuir 1938). In IR spectroscopy experiments, the ice thickness can be as thin as a few monolayers. In some cases, when ice mixtures are used, the ice has to be thicker (~3000 ML) in order to allow the detection of the less abundant molecular component in the sample or guarantee that the deposition

of background gases during the measurement is negligible (see Terwisscha van Scheltinga et al. 2018). In experiments to measure the ice refractive index, the ice thickness is generally much thicker (~45 000 ML) because the technique requires us to record several fringes in the interference pattern. It is worth mentioning that the shape and position of the IR bands are not affected by the ice thickness or the underlying substrate used in the experiments performing transmission spectroscopy.

2.2. Absorbance spectrum

The majority of the IR absorbance spectra in LIDA have been measured using transmission spectroscopy. The basic principle to measure the absorbance spectrum is that the incident radiation is attenuated when crossing the ice sample due to the intrinsic properties of the material. The intensity of the transmitted light at each wavelength (I_λ) is calculated with Lambert-Beer's law, which is given by

$$I_\lambda = I_\lambda^0 \exp\left(-\alpha_\lambda r \ell\right), \tag{1}$$

where I_λ^0 is the incident light intensity, α_λ is the wavelength-dependent absorption coefficient, r is the concentration in the sample, and ℓ is the effective radiation path within the ice. The absorbance is derived from Eq. (1) as shown below:

$$\mathrm{Abs}_\lambda = -\log_{10}\left(\frac{I_\lambda}{I_\lambda^0}\right) = 0.434 \alpha r \ell, \tag{2}$$

where the absorbance is directly proportional to the molecular concentration and the radiation path in the ice. In transmission spectroscopy, the substrate is transparent to the IR light, and the absorption bands observed in the IR spectra are due to the molecules in the ice sample.

When RAIRS is used, the absorbance is no longer obtained from Eq. (2). The absorbance spectrum is calculated as a function of the reflected light, and depending on the ice thickness, the geometry of the light path, and the setup itself, the spectrum can change substantially. Briefly, in RAIRS, the IR light shines onto a reflective gold (Au) surface at grazing angles (~90° with regard to surface normal) and is reflected toward the detector (Fig. 1b). Upon specular reflection, the s-polarized light becomes negligible, and only the p-polarized component interacts with the molecules. In this way, RAIRS has an additional selection rule for absorption, which imposes that the vibrational motions have a component orthogonal to the reflection surface (Palumbo et al. 2006). RAIRS comes with the disadvantage that spectra cannot be directly compared with astronomical data, as in the case of spectra recorded in transmission. On the other hand, RAIRS has the advantage of increasing the signal-to-noise ratio of the data.

Either transmission or RAIRS can record data of pure or mixed ices before and after warm-up, or processed by UV radiation. The ice spectrum is taken by averaging a certain number of scans, allowing a higher signal-to-noise ratio, and typical spectral resolutions are within 0.5 cm^{-1} and 2.0 cm^{-1}, whereas 0.1 cm^{-1} spectra can be recorded if needed. Likewise, the absorbance accuracy is a characteristic of the IR spectrometer and is around 1%. Warm-up experiments are performed by depositing the ice at a low temperature (~10 K), followed by a slow increase of the substrate temperature (e.g., 25 K h^{-1}) while IR spectra are continuously taken. In the cases where experiments with UV ice processing are performed, the absorbance spectrum is taken after the irradiation process. The recorded IR absorbance spectrum often shows a curved baseline, which

needs to be corrected. Typically, a low-order polynomial function is used to flatten the ice spectrum and perform corrections to remove artifacts from the IR spectra. The baseline correction is made by interpolating a function for wavelengths where there is no absorption and subtracting it from the original signal. The spectra contained in the database have previously been baseline-corrected using a polynomial or linear function to set the data to zero absorbance where there are no absorption features. When available, the non-baseline-corrected spectrum is downloadable. The original spectra (raw data) are not downloadable; this is to avoid the publication of data in the literature that have not been treated correctly. This requires appropriate knowledge of how to deal with these datasets.

For astrochemical applications, the absorbance spectrum is often converted to an optical-depth scale. The optical depth of experimental data is given by D'Hendecourt & Allamandola (1986):

$$\tau_\lambda^{\mathrm{lab}} = 2.3 \cdot \mathrm{Abs}_\lambda. \tag{3}$$

Ultimately, $\tau_\lambda^{\mathrm{lab}}$ is converted to the wave number domain (τ_ν^{lab}), and used to calculate the column density of the ice sample from the equation below:

$$N_{\mathrm{ice}} = \frac{1}{\mathcal{A}} \int_{\nu_1}^{\nu_2} \tau_\nu^{\mathrm{lab}} \mathrm{d}\nu, \tag{4}$$

in which $\mathcal{A}$ is the band strength of the vibrational modes associated with the absorption features. Most of the $\mathcal{A}$ values in the literature have been derived for pure ice samples (e.g., Gerakines et al. 1995, 1996; Kerkhof et al. 1999; Bouilloud et al. 2015; Hudson et al. 2017). However, Öberg et al. (2007) and Bouwman et al. (2007) showed that a variation in the chemical composition of the ice leads to changes in the band strength of solid-phase molecules. These changes are often reported as relative values with respect to the pure ice, because information such as the ice density is unknown when the molecular concentrations change within the ice. In Table 2, we compile $\mathcal{A}$ values from the literature for pure ices, which were then used to derive the column densities of the ices in LIDA. These values were also used to derive the column densities of most of the ice mixtures. Otherwise, we used tabulated values from Öberg et al. (2007) to derive the column densities of H$_2$O:CO$_2$, and the values from Terwisscha van Scheltinga et al. (2018, 2021), Rachid et al. (2020, 2021) to derive the column densities of ice-containing COMs.

When an ice column density is derived from RAIRS data, a correction must be performed on the band strength values from the literature. For spectra measured with RAIRS, the ice column density is given by

$$N_{\mathrm{ice}} = \frac{1}{R\mathcal{A}} \int_{\nu_1}^{\nu_2} \tau_\nu^{\mathrm{lab}} \mathrm{d}\nu, \tag{5}$$

where R is the correction factor. Specifically, in RAIRS experiments the path length of the light beam is longer across the ice than in transmission IR spectroscopy. Consequently, band strengths measured with RAIRS are no longer the same as those measured in transmission. This correction depends on the molecule and individual calibration experiments performed. Since this paper only presents results from transmission spectroscopy, the R values are not provided. Future upgrades of LIDA will include RAIRS data and their respective correction factors for the ice column density calculation.

Table 2. List of vibrational transitions and band strengths of the molecules in pure ices as included here and presented in the literature.

Molecule	λ (μm)	ν (cm^{-1})	Identification	$\mathcal{A}$ (cm mol^{-1})	References
H_2O	3.01	3322	O–H stretch	2.2×10^{-16}	Bouilloud et al. (2015)
H_2O	6.00	1666	Bend	1.1×10^{-17}	Bouilloud et al. (2015)
H_2O	13.20	760	Libration	3.2×10^{-17}	Bouilloud et al. (2015)
CO_2	4.27	2341	CO stretch	1.3×10^{-16}	Bouilloud et al. (2015)
CO_2	15.27	660, 665	bend	1.2×10^{-17}	Bouilloud et al. (2015)
CO	4.67	2141	CO stretch	1.4×10^{-17}	Bouilloud et al. (2015)
NH_3	2.96	3376	NH_3 asym-stretch	2.3×10^{-17}	Bouilloud et al. (2015)
NH_3	6.15	1624	NH_3 deformation	5.6×10^{-18}	Bouilloud et al. (2015)
NH_3	9.01	1109	NH_3 umbrella	2.1×10^{-17}	Bouilloud et al. (2015)
NH_4^+	6.85	1460	bend	4.4×10^{-17}	Schutte & Khanna (2003)
OCN^-	9.01	1109	CN stretch	1.3×10^{-16}	van Broekhuizen et al. (2005)
SO_2	7.60	1320	SO_2 stretch	3.4×10^{-17}	Boogert et al. (1997)
OCS	4.93	2025	CO stretch	3.4×10^{-17}	Rachid et al. (in prep.)
CH_4	3.32	3010	CH_4 deformation	1.1×10^{-17}	Bouilloud et al. (2015)
CH_4	7.67	1303	CH_4 deformation	8.4×10^{-18}	Bouilloud et al. (2015)
H_2CO	3.45	2891	CH_2 a-stretch	4.7×10^{-18}	Bouilloud et al. (2015)
H_2CO	3.53	2829	CH_2 s-stretch	1.3×10^{-17}	Bouilloud et al. (2015)
H_2CO	5.79	1725	C=O stretch	1.6×10^{-17}	Bouilloud et al. (2015)
CH_3OH	3.55	2816	O–H stretch	1.0×10^{-16}	Bouilloud et al. (2015)
CH_3OH	6.85	1460	O–H bend	6.5×10^{-18}	Bouilloud et al. (2015)
CH_3OH	8.85	1130	CH_3 rock	1.8×10^{-18}	Bouilloud et al. (2015)
CH_3OH	9.74	1026	C–O stretch	1.8×10^{-17}	Bouilloud et al. (2015)
HCOOH	5.85	1708	C=O stretch	5.4×10^{-17}	Bouilloud et al. (2015)
HCOOH	7.25	1384	OH bend	2.6×10^{-18}	Schutte et al. (1999)
HCOOH	8.22	1216	C–O stretch	2.9×10^{-17}	Bouilloud et al. (2015)
HCOOH	9.31	1074	CH bend	3.1×10^{-19}	Bouilloud et al. (2015)
HCOOH	10.76	929	OH bend	6.4×10^{-17}	Bouilloud et al. (2015)
CH_3CHO	5.80	1723	C–O stretch	1.3×10^{-17}	Schutte et al. (1999)
CH_3CH_2OH	9.17	1090	CH_3 rock	7.3×10^{-18}	Hudson (2017)
CH_3CH_2OH	9.51	1051	CO stretch	1.4×10^{-17}	Hudson (2017)
CH_3CH_2OH	11.36	880	CC stretch	3.2×10^{-18}	Hudson (2017)
CH_3OCH_3	8.59	1163	COC stretch + CH_3 rock	9.8×10^{-17}	Terwisscha van Scheltinga et al. (2018)
CH_3OCH_3	10.85	921	COC stretch	5.0×10^{-18}	Terwisscha van Scheltinga et al. (2018)
CH_3COCH_3	5.84	1710	C=O stretch	2.7×10^{-17}	Hudson et al. (2018)
CH_3COCH_3	7.05	1417	CH_3 a-stretch	9.2×10^{-18}	Hudson et al. (2018)
CH_3COCH_3	7.33	1363	CH_3 s-stretch	1.4×10^{-17}	Hudson et al. (2018)
CH_3COCH_3	8.14	1228	CCC a-stretch	7.3×10^{-18}	Hudson et al. (2018)
CH_3COCH_3	18.79	532	CO deformation	2.1×10^{-18}	Hudson et al. (2018)
CH_3OCHO	5.80	1723	C=O stretch	5.0×10^{-17}	Modica & Palumbo (2010)
CH_3OCHO	8.25	1211	C–O stretch	2.9×10^{-17}	Modica & Palumbo (2010)
CH_3OCHO	8.58	1165	CH_3 rock	2.0×10^{-17}	Modica & Palumbo (2010)
CH_3OCHO	10.98	910	O–CH_3 stretch	4.8×10^{-18}	Modica & Palumbo (2010)
CH_3OCHO	13.02	768	OCO deformation	1.2×10^{-18}	Modica & Palumbo (2010)
CH_3NH_2	3.47	2881	CH_3 a-stretch	2.6×10^{-18}	Rachid et al. (2021)
CH_3NH_2	3.58	2791	CH_3 s-stretch	3.8×10^{-18}	Rachid et al. (2021)
CH_3NH_2	6.76	1478	CH_3 a-deformation	1.1×10^{-18}	Rachid et al. (2021)
CH_3NH_2	6.87	1455	CH_3 a-deformation	7.0×10^{-19}	Rachid et al. (2021)
CH_3NH_2	7.024	1420	CH_3 s-deformation	2.0×10^{-19}	Rachid et al. (2021)
CH_3NH_2	8.63	1159	CH_3 rock	1.5×10^{-18}	Rachid et al. (2021)
CH_3CN	3.33	3001	CH_3 a-stretch	1.5×10^{-18}	Rachid et al. (2022)
CH_3CN	3.40	2940	CH_3 s-stretch	5.3×10^{-19}	Rachid et al. (2022)
CH_3CN	4.44	2252	CN stretch	1.9×10^{-18}	Rachid et al. (2022)
CH_3CN	7.09	1410	CH_3 a-deformation	1.90×10^{-18}	Rachid et al. (2022)
CH_3CN	7.27	1374	CH_3 s-deformation	1.2×10^{-18}	Rachid et al. (2022)
CH_3CN	9.60	1041	CH_3 rock	1.6×10^{-18}	Rachid et al. (2022)
CH_3CN	10.88	919	CC stretch	3.5×10^{-19}	Rachid et al. (2022)
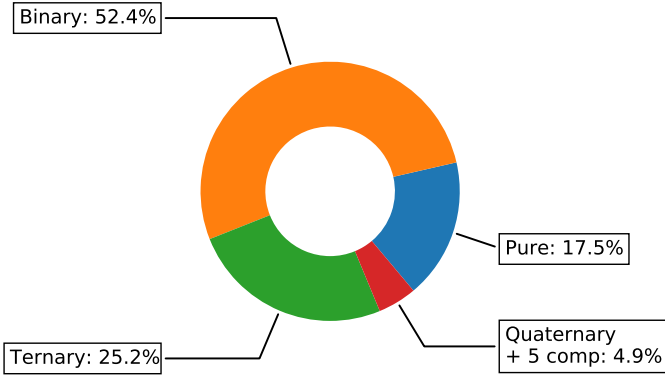
Fig. 2. Pie chart displaying the percentage division of ice analogs in LIDA from pure samples to five-component mixtures.

Spectra of mixed ices are shown in the database, with the ratio between the molecules given in the label. For example, in the $H_2O:CO_2$ (10:1) ice there are ten molecules of H_2O for each molecule of CO_2 in the ice. Layered ices can also be made by depositing a certain number of monolayers (1 monolayer - ML $\sim 10^{15}$ molecules cm^{-2}) of a pure molecule on the substrate followed by a number of ML of another pure or mixed ice. When this is the case, the mixture is named "CO over CO_2", which means that pure CO was deposited on top of a pure CO_2 ice. Similarly, "CO under CO_2" means that CO was deposited in the bottom layer, followed by CO_2 deposition on the top layer.

In Fig. 2, we show the fraction of pure and mixed samples hosted in LIDA. The majority of the IR spectra are of binary ice samples accounting for 52.4%. Most of these samples are mixtures of simple molecules (e.g., H_2O, CO, CO_2). Recently, binary ices containing COMs (e.g., CH_3CHO, CH_3CH_2OH, CH_3OCH_3, CH_3NH_2, CH_3OCHO, CH_3COCH_3, CH_3CN) have been included in the database. The second biggest group (25.2%) is of ice samples containing three compounds, which may include a COM. Pure ice samples make up the third group (17.5%) and contain simple and complex molecules, as well as ions (NH_4^+ and OCN^-). We note, however, that these ions are formed via the heating of $HNCO:NH_3$ ice (Novozamsky et al. 2001). Moreover, some of the pure ice samples were exposed to UV radiation with experimental details given in Gerakines et al. (1996). Finally, the groups of quaternary and five-component ice samples are combined and account for 4.9% of all spectra in the database. A full list with all ice analogs in the database is presented in Table A.1.

2.3. UV/visible and mid-IR refractive index

When light shines upon the ice surface, part of it refracts into the ice, and part of it is specularly reflected by the surface (Figs. 1c and d). The refracted beam is reflected in the ice-substrate interface and eventually emerges back into the vacuum. The phase difference (Δ) between the light rays that pass through the ice and the ones reflected by the surface is related to their optical path difference (δ), which is given by

$$\Delta = \frac{2\pi}{\lambda}\delta, \tag{6a}$$

$$\delta = 2nd\cos(\theta_2), \tag{6b}$$

where λ is the wavelength of the incoming light, n is the real part of the ice refractive index at wavelength λ, d is the ice thickness, and θ_2 is the refraction angle (see Fig. 1c), that is the angle

between the refracted light and the normal plane perpendicular to the ice. The incident angle θ_1 is related to the refraction angle θ_2 by Snell's law. When δ/λ is an even number, Δ is a multiple of 2π, resulting in constructive interference of the light beams. Conversely, when δ/λ is an odd number, the interference is destructive. Consequently, the intensity of the resulting beam reflected by the ice surface is an oscillation pattern with the following form:

$$\begin{aligned} I(t) &= A + B\cos[\Delta(t)] \\ &= A + B\cos\left(\frac{4\pi nd(t)\cos(\theta_2)}{\lambda}\right), \end{aligned} \tag{7}$$

where A and B are constants. Thus, the intensity of the interference pattern carries information about both the refractive index and the rate at which the ice thickness increases during deposition. Since each of these parameters is unknown, they cannot be derived from a single interference measurement. However, by recording the interference pattern of growing ice employing two different incident angles or wavelengths and employing Eq. (7), both the ice refractive index and the growth rate can be derived. By recording the interference pattern of growing ice using two light beams of the same wavelength (λ) but different angles (α, β), the refractive index expression can be derived from the frequency of the oscillations (Eq. (7)) and Snell's law:

$$n_{UV-vis} = \sqrt{\frac{\sin^2\alpha - (P_\beta/P_\alpha)^2\sin^2\beta}{1 - (P_\beta/P_\alpha)^2}}, \tag{8}$$

where P_α and P_β are the periods of the interference patterns generated by the light beams striking the ice at angles α and β, respectively. For more details about the derivation of Eq. (8), see, for example, Tempelmeyer & Mills Jr (1968), Beltrán et al. (2015), and He et al. (2022).

While Eq. (8) provides the ice refractive index in the UV/vis range, the refractive index in the mid-IR can be calculated using the Kramers-Kronig relations (Kronig 1926; Kramers 1927), which are given by

$$n(\nu) = n_{670\,nm} + \frac{2}{\pi}\mathcal{P}\int_{\nu_1}^{\nu_2}\frac{\nu'k(\nu')}{\nu'^2 - \nu^2}d\nu', \tag{9}$$

where $n_{670\,nm}$ is the refractive index of the sample at 670 nm and is within the UV/vis range for which the refractive index was derived (through Eq. (8)), ν is the wave number corresponding to the peak of the band, and ν' is the wave number before and after the ν value. The Cauchy principal value $\mathcal{P}$ is used to overcome the singularity when $\nu = \nu'$. The term "k" corresponds to the imaginary part of CRI and is given by

$$k = \frac{1}{4\pi\nu d}\cdot\left(2.3\times Abs_\nu + \ln\left|\frac{\tilde{t}_{01}\tilde{t}_{02}}{1 + \tilde{r}_{01}\tilde{r}_{12}e^{2i\tilde{x}}}\right|^2\right), \tag{10}$$

where Abs_ν is the absorbance spectrum value (Eq. (2)), d is the thickness of the ice sample, and $\tilde{t}_{01}$, $\tilde{t}_{02}$, $\tilde{r}_{01}$, and $\tilde{r}_{12}$ are the Fresnel coefficients. The sub-labels 0, 1, and 2 refer to vacuum, ice sample, and substrate regions, respectively. The refractive index of the substrate is implicit in the terms $\tilde{t}_{02}$ and $\tilde{r}_{12}$. Finally, the term $\tilde{x}$ is given by $\tilde{x} = 2\pi\nu d\tilde{m}$; $\tilde{m}$ is the CRI.

To determine the real and imaginary refractive index in the mid-IR, LIDA provides tools to solve Eqs. (9) and (10) numerically via an iterative procedure. Specifically, LIDA uses the Maclaurin formula described in Ohta & Ishida (1988) to

obtain the real refractive index, and, subsequently, the imaginary refractive index is derived. This methodology was also employed in other computational codes dedicated to calculating the CRI values of ice samples (Rocha & Pilling 2014; Gerakines & Hudson 2020).

In the current version of LIDA, we present the H_2O ice refractive index in the UV/vis, measured on the OASIS setup, and mid-IR optical constants calculated with the online tool available in LIDA (see Sect. 4.2). In a follow-up paper, the refractive indexes of pure H_2O shown in this database will be systematically compared with the literature values (Rocha et al., in prep.). The refractive index values of other molecules (e.g., CO, CO_2, N_2, CH_4, CH_3OH) have in part already been measured and will be included in future LIDA upgrades. These will also include astronomically relevant ice mixtures.

3. Features of the database

The upgraded LIDA is an extendable platform designed to host IR spectra and UV/vis refractive indices of ice samples, as well as to support the uploading of new datasets that will be obtained in future experiments. Access to these data is obtained with dynamical and interactive visualization software that is also linked to online tools to perform astronomy-oriented calculations. Additionally, all data are available for download in a standard ascii format. In the next subsections, we provide details about different aspects of the database. More information describing the software and approaches used to construct the database are given in Appendix B and interactive documentation is available in the online documentation[16].

3.1. User interface

The user interface of LIDA shows four sub-modules, namely, (i) spectral data, (ii) optical constants, (iii) online tools, and (iv) further information and a contact form. Access to these sub-modules is obtained via the navigation bar at the top of the web interface. All IR ice spectra are available in the sub-module named spectral data, which currently counts for more than 1100 ice spectra related to over 150 different ice samples. In the future, new data will be added, and the option exists to add previously recorded data that are currently scattered over the literature. The "optical constants" section only contains the real refractive index of H_2O ice at different temperatures for now. However, more data from ongoing experiments will be added, which includes measurements of N_2, CO, CO_2, CH_4, and CH_3OH. LIDA is also equipped with *online tools* focused on astronomy-oriented calculations. Finally, the user can visualize the credits, and contact the developers and scientific managers of the database. To render the database user interface, we used common web technologies such as HyperText Markup Language (HTML), Cascading Style Sheets (CSS), and JavaScript (JS). A list of all software used to develop LIDA is available at the "credit" section[17] of LIDA.

3.2. Search capability and metadata

The IR spectra and the UV/vis optical constants of the ice analogs in LIDA can be searched via a search box by accessing the spectral data and optical constants tabs, respectively, in the navigation bar. The search capability uses SQLAlchemy[18], a python SQL (Structured Query Language) toolkit, and Object Relational Mapper to enable searches in `Flask` applications.

To find a specific analog in the database, either the chemical formula or the molecule name can be used. For example, the user can type `water` or `H2O` to search for water ice spectra in the database. Searching for ice mixtures is possible by providing a list of the chemical formulas separated by a space (e.g., `H2O CO2 CH3OH`). LIDA can also be used to search for molecules sharing common chemical structures. For example, when the query is `CO`, a list of all the molecules containing a carbon-oxygen bond (both simple and double) will be displayed on the web interface (e.g., CH_3OH, CH_3CHO, HCOOH). Searching for more specific structures, such as functional groups, is also possible. As an example, if the query is `COOH`, a list with samples containing molecules that carry a carboxylic acid functional group will be returned (e.g., HCOOH). LIDA also supports searching by the type of ice processing. For example, thermally processed water ice can be searched for with `H2O category=warm-up`. Similarly, an energetically processed ice can be searched for with `H2O category=irradiation`. Finally, the user can also search for a spectrum by the author who published the data with the command `H2O author=Öberg`.

By searching for a specific ice sample, the user can also visualize the metadata. For example, information such as spectral resolution, deposition temperature, ice thickness, and publication are visible. All spectra hosted in LIDA are available for download in ascii format (e.g., `.txt` extension), which is a standard format that can be imported to several software and computational codes. This feature enables the downloading of a single spectrum or all spectra related to an ice analog.

3.3. Data visualization

The data in LIDA are plotted interactively with `Bokeh`[19], a Python library for interactive visualization (Bokeh Development Team 2018). This software provides several control buttons by default to support the interactive inspection of the plots. More details can be accessed via the `Bokeh` documentation.

As an example of the data visualization in LIDA, Fig. 3 shows the IR absorbance spectrum of pure H_2O ice at temperatures of 15, 45, 75, 105, and 135 K (Öberg et al. 2007). The color of each spectrum is linked to the temperature for which the data was recorded; in this case, blue and red are the lowest and highest temperatures, respectively. The spectral visualization in LIDA also contains the annotations for the vibrational modes of the molecule. Four spectral features are indicated for H_2O ice. The feature around 3800 cm^{-1} (2.63 μm) corresponds to the free OH stretching or dangling bond. This band is often observed in amorphous water ice, and decreases upon compaction after ion irradiation of the ice as shown by Palumbo (2006). However, Bossa et al. (2014, 2015) suggest that the OH dangling bond is only a partially suited tracer of ice porosity, as a non-detection does not fully exclude that an ice is still somewhat porous. After the ice is warmed up, the dangling bond is no longer observed in this water ice spectrum. The most prominent feature is the absorption band around 3300 cm^{-1} (3 μm), which refers to the OH bulk stretching in the ice. This band is broad and relatively symmetric at low temperatures, whereas it becomes narrow and sharp at higher temperatures. This variation in the shape of the

---
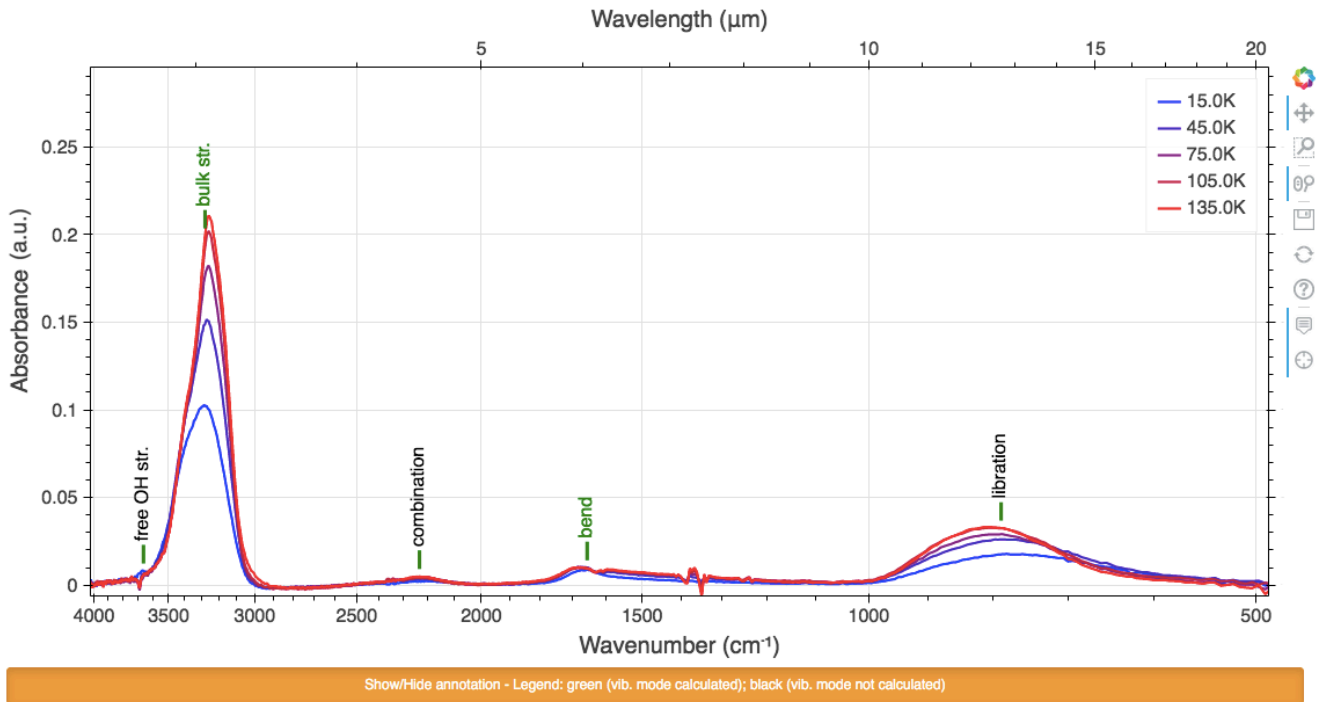
Fig. 3. Screenshot of spectrum visualization window showing IR spectrum of H_2O ice at different temperatures given by the color-code. The annotations of the water vibrational modes are shown in green. They can be hidden by clicking on the yellow toggle below the plot. It also describes the annotation color-code; green means the vibrational mode is calculated, and black indicates the vibrational mode is not calculated. The hover set at the position around 3000 cm^{-1} displays the information of the spectral data point, such as the wave number in cm^{-1} (*bottom X-axis*), wavelength in μm (*top X-axis*), and absorbance (*Y-axis*). The toolbar is placed on the right side of the plot.
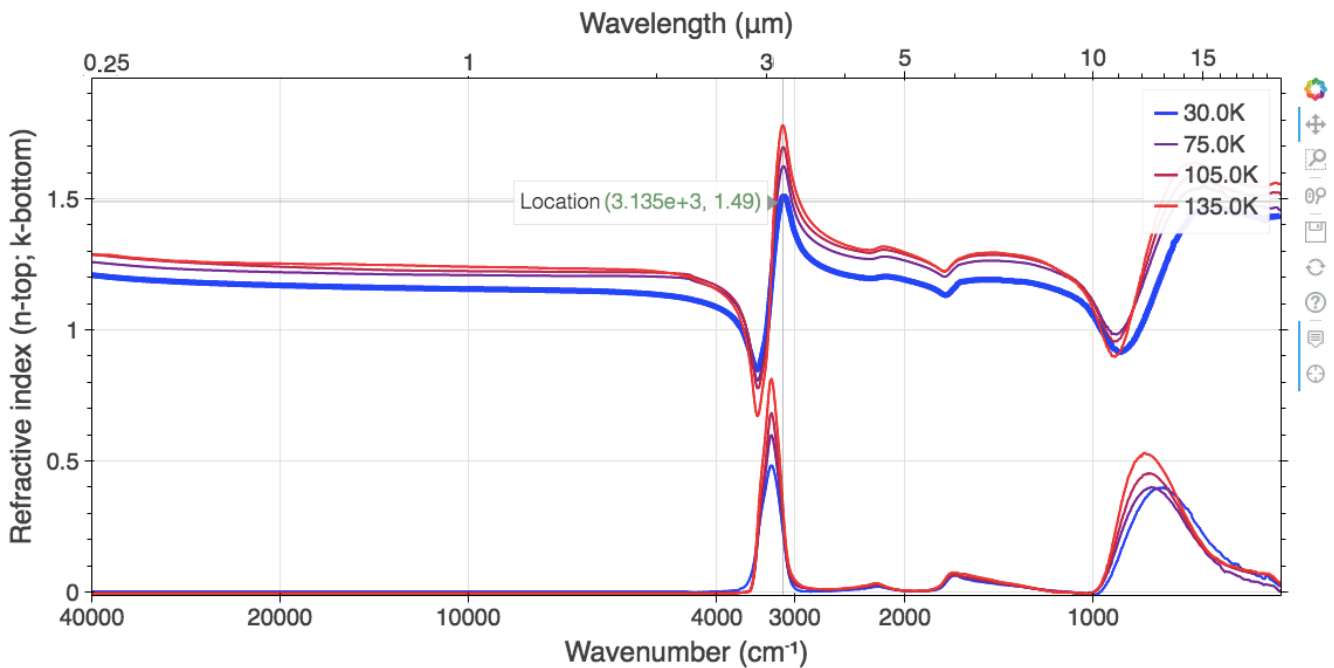
Fig. 4. Screenshot showing UV/vis and mid-IR refractive index of pure H_2O at different temperatures. The color is associated with the temperature of the ice. The hover shows the wave number in cm^{-1} and refractive index values as indicated in this figure.

band is due to the phase transition of water ice from the amorphous to the crystalline structure. The water bending mode is observed at 1666 cm^{-1} (6 μm). The effect of the temperature on this feature is the flattening of the band during heating. Finally, the libration water band is observed around 800 cm^{-1}. The peak

position of this band is also sensitive to the physical conditions of the ice and is blueshifted at higher temperatures.

In Fig. 4, we display the UV/vis and mid-IR refractive indices (0.25–20 μm) of pure H_2O ice at 30, 50, 100, and 150 K. The UV/vis was measured on the OASIS setup (He et al. 2022),
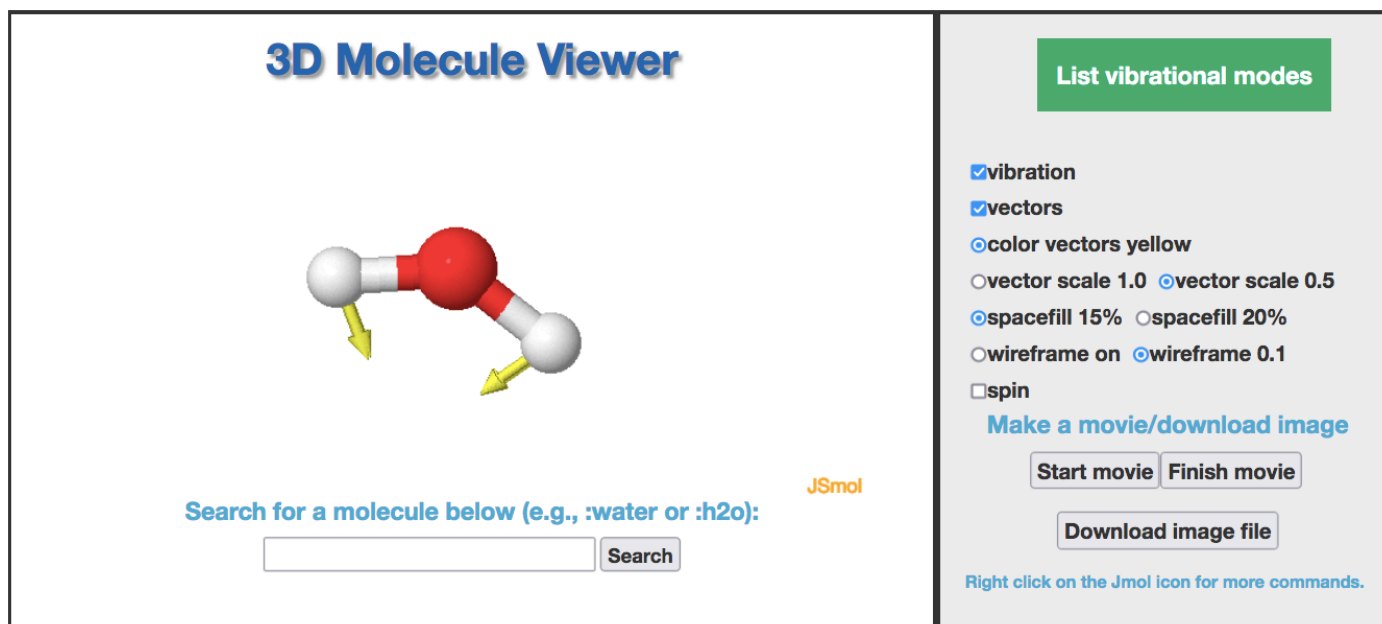
Fig. 5. Screenshot of three-dimensional (3D) molecule viewer embedded in LIDA using the `JSmol` package. The viewer is connected to external public databases of molecule structures and can be viewed using the searching bar below the molecules. A few dedicated controls can be used to move and animate the molecule. The calculated vibrational modes can be listed and animated using the green button. As proof of concept, the yellow arrows indicate the vibrational motion of the water bending mode seen at 1643 cm^{-1} in Fig. 3. Buttons for making a movie and downloading the image file in PNG format are also provided.

whereas the mid-IR values were calculated using the refractive index calculator available via LIDA (see Sect. 4.2). The water ice refractive index shows a clear dependence on the temperature. In particular, the real refractive index at 670 nm is adopted as 1.29 and 1.32 for the amorphous and crystalline phases, respectively (e.g., Warren 1984; Hudgins et al. 1993; Mastrapa et al. 2008, 2009), which are higher than the values presented in this paper.

3.4. 3D molecule viewer

The 3D molecule viewer aims to provide complementary information about the molecules in the ice analogs available through LIDA. The viewer is built with `Jmol`[20], an open-source Java package for the visualization of chemical structures in 3D (Jmol development team: Accessed in June 2021). The web rendering of the viewer is done via `JSmol`, an interactive browser object that is written in JavaScript and utilizes `HTML5`.

`JSmol` has several built-in functions that are also available in this tool, such as measurements of distances and angles and the visualization of vibrational modes, animations, orbitals, and surfaces. As a 3D viewer, the molecule can be rotated to different angles, and the type of the bonds can be changed to wire frames. A few dedicated controls are available in the viewer of LIDA; for example, "spin" to rotate the molecule, "vibration" to show an animation of the vibrational modes and "vectors" to show the direction of the vibration modes of the functional groups. All these capabilities are important for a better understanding of the spectroscopic properties of the molecules available in LIDA. It should be noted that in the ice environment molecular rotations are quenched and vibrations are hindered depending on the ice matrix. Furthermore, the ice geometry changes with the variation of the temperature and upon irradiation, which also affects the molecular vibrations.

With `JSmol` linked to LIDA, one can animate the normal vibrational modes of the molecules when visualizing their IR ice spectra. This is performed by reading ".xyz" via `JSmol`, which contains information about the molecular geometry in Cartesian coordinates, as well as the normal frequencies of the vibrational modes. The default `JSmol` buttons to control the vibrational mode animations are disabled when the ".xyz" is not available yet in LIDA. In Sect. 3.5, we provide further details about the calculation of the vibrational modes used in the database. This viewer only shows one molecule per ice analog. This means that for an ice mixture such as $H_2O:CH_3CH_2OH$, only the H_2O molecule is immediately displayed in the viewer. To allow the user to visualize other molecules (e.g., CH_3CH_2OH), the 3D Molecule Viewer is linked to PubChem[21] (Bolton et al. 2011; Kim et al. 2020), there is a comprehensive database of freely accessible chemical information maintained by the National Center for Biotechnology Information (NCBI). Searching for a molecule is as simple as typing `:ethanol` to visualize the 3D shape of CH_3CH_2OH. The colon symbol ":" provides the key to connect with the PubChem database. These databases contain detailed information on several molecules, which can help the user to understand different aspects of the molecular properties. Figure 5 shows an example of the 3D molecule viewer, which displays a screenshot of the bending mode animation of the H_2O molecule.

3.5. Vibrational mode calculation

The vibrational modes of the molecules in LIDA are calculated with the ORCA[22] software (Neese 2012, 2018; Neese et al. 2020), which contains a wide variety of quantum chemistry methods for different purposes. In the 2022 release of LIDA, the aim of the calculation of the vibrational modes is to show the animation

---

[20] http://jmol.sourceforge.net/

[21] https://pubchem.ncbi.nlm.nih.gov/
[22] https://orcaforum.kofo.mpg.de

of the vibrational modes, and, therefore, the focus is not on the accuracy of the vibrational frequencies. These have to be taken from experimental values. For the calculations, it is assumed that a molecule is isolated, not in a matrix surrounded by other molecules, and it is in the electronic ground state. In addition, ORCA considers that all vibrations are strictly harmonic. The consequence of such approaches is that the wave numbers of some vibrational modes calculated with ORCA deviate from the wave numbers of the absorption bands observed in experimental IR spectra or may even be completely absent. The numerical error in the calculation of vibrational frequencies with ORCA may be as large as 50 cm^{-1}, although it is considerably lower in most of the cases. Nonetheless, vibrational mode assignments are correct and can be used as a tool to visualize the animation of the molecular motions.

For the molecule geometry optimization and calculation of the vibrational modes, we adopt the density functional theory (DFT) with the functional B3LYP, which stands for Becke, 3-parameter, Lee-Yang-Parr" (Becke 1993; Stephens et al. 1994). The input geometry of the molecules is taken from the PubChem database. The vibrational frequencies calculated for the molecules in the database can be visualized in the 3D molecule viewer described in Sect. 3.4. Additionally, the modes with calculated frequencies are indicated in green in the annotations of the spectrum visualization. Rotational transitions are not available in these files because they are quenched in the ice environment.

4. Online tools and applications

In this section, we introduce two new online tools focused on the creation of synthetic spectra using the laboratory data from the database and the derivation of the CRI at IR wavelengths of ice samples. These tools also have an intuitive graphical user interface that makes it easier to use and download the output results. The details are given in the subsections below.

4.1. SPECFY

SPECFY is an online tool available through LIDA to construct synthetic spectra of protostars containing ice absorption bands. This tool uses Python `Flask` to render the web page and `JavaScript` to show the absorbance spectra in a drop-down menu to be used by SPECFY. The web interface of SPECFY is shown in Appendix C.1. The next subsections describe the tool and show practical applications of how to use SPECFY to interpret astronomical observations.

4.1.1. Synthetic spectra

To construct a synthetic spectrum with multiple ice features, SPECFY performs a linear combination of experimental data in LIDA that is available via a drop-down menu on the web interface. The linear combination is given by

$$\tau_\lambda^{tot} = \sum_{i=0}^{n} w_i \tau_{\lambda,i}^{lab},$$ (11)

where w_i is the weighting factor used to increase or decrease the intensity of the ice bands, and $\tau_{\lambda,i}^{lab}$ is calculated with Eq. (3). The weighting factor w_i is calculated by the following equation:

$$w_i = \frac{N_{ice}^{inp}}{N_{ice}^{lab}},$$ (12)

where N_{ice}^{inp} is the input ice column density provided by the user in LIDA, and N_{ice}^{lab} is the ice column density of the sample itself, which is calculated with Eq. (4). For example, if the user requires a column density of 10^{18} cm^{-2} and the experimental spectrum has a column density of 10^{17} cm^{-2}, the selected spectrum will be multiplied by a factor of 10 in Eq. (11). It is worth noting that all experimental data are interpolated during the linear combination to ensure consistency of the method and avoid spectral range variations of the input data.

Besides the ice spectra hosted in LIDA, the template amorphous silicate spectrum of the galactic center source GCS 3 taken from Kemper et al. (2004) is also available to be combined with the ices. This spectrum was observed with ISO towards the Galactic center and has been used as a template to remove the silicate features observed toward protostars in previous works (e.g., Boogert et al. 2008; Bottinelli et al. 2010). In LIDA, this silicate spectrum is important for synthetic spectrum calculations because it makes it possible to check the effects of the Si–O bands when blended with ice absorption features. However, we stress that no mixing rule, such as the theories of Maxwell Garnett (Garnett 1904, 1906) and Bruggeman (Bruggeman 1935, 1936), is assumed in this procedure. In practice, SPECFY assumes isolated materials. Additionally, this tool does not include secondary effects of grain size and geometry or scattering processes that might affect the shape of the ice bands. Those features will be included in future work dedicated to improving SPECFY.

The combined ice spectrum can be used to match observational data. As an example, we created a synthetic spectrum using the parameters described in Table 3. The results are shown in Fig. 6 and the outputs in the web interface of SPECFY are displayed in Fig. C.2. The LIDA model in optical depth scale is constructed with SPECFY by combining ice and silicate spectra with different input column densities. The ice components in this combination are composed of pure H_2O at 15 K and the mixtures $H_2O:CO_2$ (10:1) and $CO:CO_2$ (2:1). These three ice samples comprise the most abundant ice molecules observed toward protostars (Öberg et al. 2011; Boogert et al. 2015). Superposed in relation to the LIDA model, we display the spectrum of the protostar AFGL 989, observed with *ISO* (Gibb et al. 2004). The good agreement between the model and the strong bands in observations show that SPECFY is a useful tool for modeling astronomical data. This solution is not necessarily unique to the AFGL 989 spectrum, but this methodology provides the means to help in the quantification of the ice column densities as well as the interpretation of astronomical observations.

The $H_2O:CO_2$ ice mixture dominates the absorption profile of the band at 3 μm, but it cannot fully explain the absorption excess of the spectral red wing region of AFGL 989. The nature of this strong absorption profile is under debate, but it is often attributed to scattering due to large grains (e.g., Boogert et al. 2000) and ammonia hydrates ($H_2O:NH_3$; e.g., Merrill et al. 1976; Dartois et al. 2002). The water ice bending and libration modes are also observed around 6 μm and 13.6 μm. Likewise, the CO_2 bands at 4.27 μm and around 15 μm are not entirely modeled by the carbon dioxide fraction in the $H_2O:CO_2$ mixture. Additional CO_2 is added by the $CO:CO_2$ ice mixture. A fraction of carbon monoxide is expected to coexist in the ice matrix of carbon dioxide, as indicated in astronomical observations (Pontoppidan et al. 2008; Poteet et al. 2013). Although this combination matches the two CO_2 bands relatively well, it results in a higher CO ice peak at 4.67 μm. Finally, the absorption profile of the silicate is relatively well reproduced with the amorphous silicate of GCS 3. Similarly to the unclear origin of the absorption excess around

Table 3. Continuum SEDs available in the SPECFY tool compiled from Gibb et al. (2004) and Boogert et al. (2008).

Protostar	Continuum model (Jy)	Continuum method [a]	Observations
Class I (disk, envelope)			
Elias 29	B2000	Blackbody	ISO/SWS
AFGL 989	G2004	Polynomial + Blackbody	ISO/SWS
CrA IRS7 A	B2008	Polynomial	ISAAC/VLT & *Spitzer*/IRS
CrA IRS7 B	B2008	Polynomial	ISAAC/VLT & *Spitzer*/IRS
IRAS 23238+7401	B2008	Polynomial	NIRSPEC/Keck & *Spitzer*/IRS
L1014 IRS	B2008	Polynomial	NIRSPEC/Keck & *Spitzer*/IRS
Transition from Class I to Class II (disk, tenuous envelope)			
DG Tau B	B2008	Polynomial	NIRSPEC/Keck & *Spitzer*/IRS
CRBR 2422.8-3423	B2008	Polynomial	NIRSPEC/Keck & *Spitzer*/IRS

Notes. [a]Polynomial: low-order (≤ 3) polynomial function. Blackbody: a single or multiple blackbody curves to fit the local continuum adjacent to the ice absorption features.

Table 4. Selected ice spectra and continuum model to construct a synthetic protostar spectrum. For an example, see Fig. 6.

Analog	T (K)	N_{ice}^{inp} (cm^{-2})	Reference
Spectrum selection			
Pure H$_2$O	15	1.4×10^{17}	Öberg et al. (2007)
H$_2$O:CO$_2$ (10:1)	10	2.5×10^{18}	Ehrenfreund et al. (1997)
CO:CO$_2$ (2:1)	15	7.0×10^{17}	van Broekhuizen et al. (2006)
Silicate GCS 3	...	1.0×10^{20}	Kemper et al. (2004)

Object	Continuum model	Flux unit	Reference
Continuum selection			
Elias 29	B2008	Jansky	Boogert et al. (2008)
AFGL 989	G2004	Jansky	Gibb et al. (2004)
DG Tau B	B2008	Jansky	Boogert et al. (2008)

Notes. All data are interpolated in the range between 2.6 and 20 μm.

3.3 μm, other strong absorptions are observed at 6 μm, which are usually associated with organic refractory material (Gibb & Whittet 2002; Boogert et al. 2008), and at 6.85 μm, often attributed to CH$_3$OH (Bottinelli et al. 2010, e.g.,) and NH$_4^+$ (e.g., Keane et al. 2001; Schutte & Khanna 2003; Maté et al. 2009, 2012). This exercise shows that the resources available in LIDA can be used to analyse the spectra of protostars and obtain ice column densities.

Next, the optical depth spectrum can be converted to a flux scale in Jy units by adopting the continuum SEDs of different protostars. We compiled and added the continuum SED of seven protostars as calculated by Gibb et al. (2004) and Boogert et al. (2008) to LIDA; these are listed in Table 4. The sources are representative of Class I and Class II objects and have spectral data obtained with ground- and space-based telescopes. Except in the cases of Elias 29 and AFGL 989, which were observed with the ISO/short-wavelength spectrometer (SWS) in the entire range between 2 and 30 μm, all sources have coverages of 2.5–5 μm (except 4.0–4.4 μm) and 5–30 μm. The former interval is based on the VLT/ISAAC observations summarized in Pontoppidan et al. (2003) and van Broekhuizen et al. (2005) or Keck NIRSPEC (McLean et al. 1998) observations. The latter range is constrained by space-based observations with the Infrared Spectrograph (IRS) of the *Spitzer* Space Telescope. Despite the careful SED determination by Gibb et al. (2004) and

Boogert et al. (2008), inaccuracies may still occur, and this must be taken into account when using these data. Once the continuum SED is known, it can be used to convert the ice's experimental spectra from optical depth to a flux scale. The conversion to the synthetic spectrum in flux scale is performed as follows:

$$F_\lambda^{synth} = F_\lambda^{cont} \exp(-\tau_\lambda^{tot}), \qquad (13)$$

where F_λ^{cont} is the continuum SED of the protostar.

Figure 7 shows three synthetic spectra using the continuum templates from AFGL 989, Elias 29, and DG Tau B, which represent three protostar categories, a high-mass protostar, a low-mass protostar, and a protoplanetary disk, respectively. The continuum applied to the optical depth model is displayed in Fig. 6 and the output in the web interface is displayed in Fig. C.2. The effect of the continuum in this example is characterized by different flux intensities and by changing the slope of the protostar SED. Additionally, Fig. 7 shows the sensitivity limits for the filters G235M and G395M of the JWST/Near-Infrared Spectrometer integral field unit (NIRSpec/IFU) and all filters of the Mid-Infrared Instrument at Medium Resolution Spectroscopy (MIRI/MRS). These values represent the minimum detectable signal corresponding to a signal-to-noise ratio of 10 obtained with an on-source integration time of 10 000 seconds (Glasse et al. 2015; Pontoppidan et al. 2016). This comparison shows that
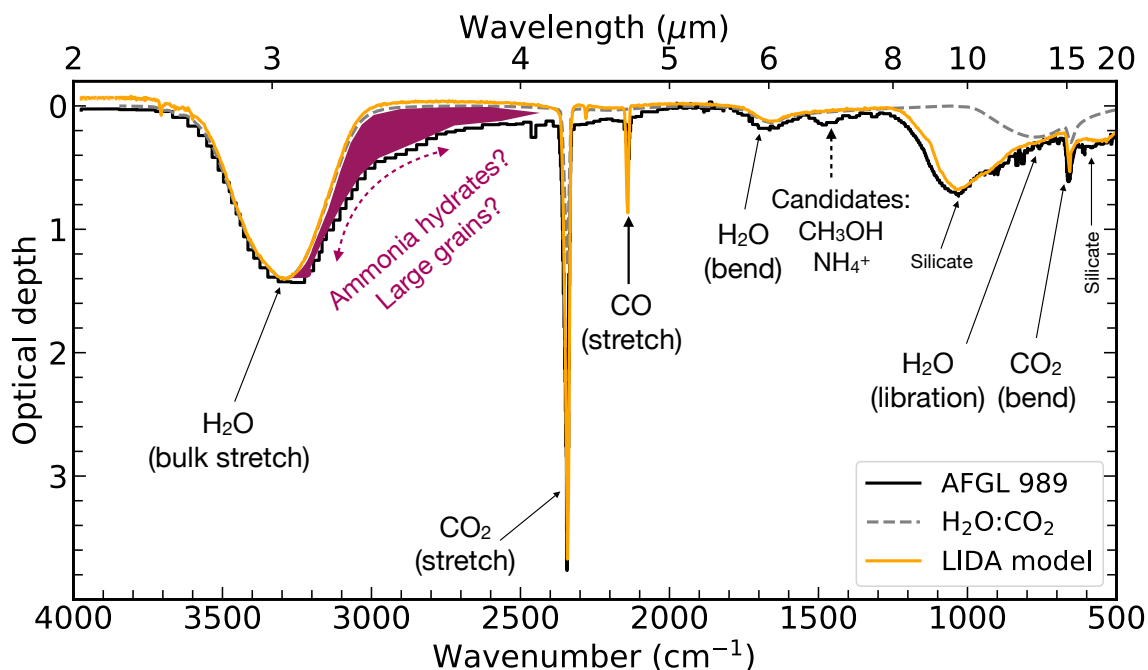
Fig. 6. AFGL 989 vs. LIDA model. LIDA model using the SPECFY online tool (orange) superposed to the ISO spectrum of the protostar AFGL 989 (black) in the optical depth scale taken from Gibb et al. (2004). The synthetic spectrum in the optical depth scale is composed of the linear combination of three ice spectra (pure H_2O, $H_2O:CO_2$ (10:1), and $CO:CO_2$ (2:1)) and silicate template from the GCS 3 source. The dominant ice spectrum is $H_2O:CO_2$ (10:1), shown by the gray dashed line. The assignments of a few bands are indicated. The red hatched area highlights an infrared absorption excess attributed to ammonia hydrates and large grains (see text).
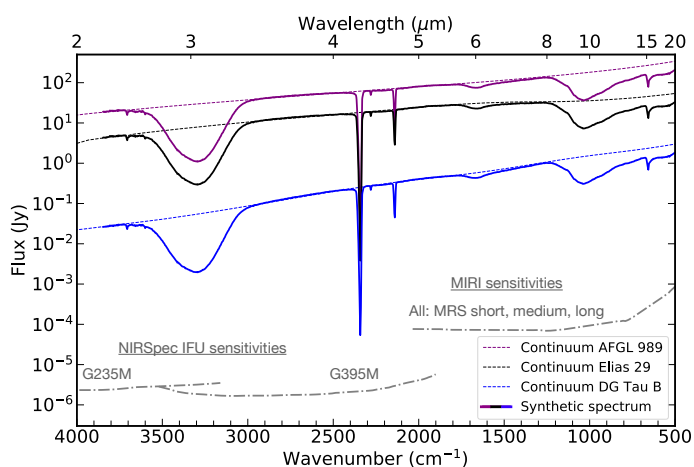
Fig. 7. Output spectra (solid lines) from SPECFY in Jy showing the effect of selecting different continuum SED templates (dashed lines). The sensitivities of JWST/NIRSpec medium resolution and MIRI for 10 000 s integration time are shown for comparison by the gray dot-dashed lines.

ices can be easily detected with the JWST toward sources with continuum SEDs similar to AFGL 989, Elias 29, and DG Tau B. With this feature in LIDA, one can generate input spectra for the JWST Time Exposure Calculator[23] (ETC) that can be used in future proposals cycles.

4.1.2. Functional groups in protostellar spectra

LIDA also has the capability of searching for molecules containing similar associations of atoms and some functional groups,

as described in Sect. 3.2. Once these are chosen, one can select them from the drop-down menu in SPECFY to construct a model spectrum for comparison with the observations. A practical example is given in Fig. 8. We use two separate entries (CO and CH) in the "spectral data" field of LIDA to search for molecules sharing carbon-oxygen bonds (e.g., carbonyl-bearing molecules, alcohols) and carbon-hydrogen bonds as shown in the top panel of Fig. 8. From the CO entry, several ice analogs are found, including HCOOH, CH_3OH, CH_3CHO, and CH_3COCH_3. Similarly, the CH entry returns the same molecules because they contain CO and CH chemical bonds. In addition, LIDA also finds CH_4 based on the query request.

The vibrational modes of functional groups containing a carbonyl group, C–O and C–H bonds have been assigned to the spectra of protostars (e.g., Gibb et al. 2004; Boogert et al. 2015). To illustrate how LIDA can further support astronomical data interpretation, in the middle panel of Fig. 8, we show the experimental spectra of HCOOH, CH_3CHO, CH_3OH, CH_3COCH_3, and CH_4 scaled to the spectra of the low-mass protostar HH46 (Boogert et al. 2008). The HH46 spectrum is subtracted of the water ice and silicate. The chemical bonds associated with the absorption bands are indicated in the green and blue shaded areas. The bottom panel of Fig. 8 highlights the chemical bonds of the molecules contributing to the absorption bands toward HH46. The parameters used to scale laboratory data to the observations are given in Table 5. This exercise shows that LIDA can be used to identify the chemical bonds related to different absorption bands and provide upper-limit column densities for ices. Figure 8 also highlights the blending of bands at different spectral regions. For example, the C=O stretching modes of HCOOH, CH_3CHO, and CH_3COCH_3 lie almost at the same wavelength, which hints at the need for high-sensitivity and spectral-resolution observational data that will be provided by the JWST. Clearly, this is an important tool to explore the

---

[23] https://jwst.etc.stsci.edu/

Table 5. Ice spectra selected from LIDA entries `CO` and `CH` and their column densities after manually scaling to HH46 spectrum shown in Fig. 8.

Analogue	T (K)	N_{ice}^{inp} (cm^{-2})	Reference
Pure HCOOH	15	1.9×10^{17}	Bisschop et al. (2007)
Pure CH$_3$CHO	15	6.1×10^{17}	Terwisscha van Scheltinga et al. (2018)
Pure CH$_3$COCH$_3$	15	1.7×10^{17}	Rachid et al. (2020)
Pure CH$_3$OH	15	7.7×10^{17}	Fraser & van Dishoeck (2004)
Pure CH$_4$	15	1.4×10^{17}	Fraser & van Dishoeck (2004)
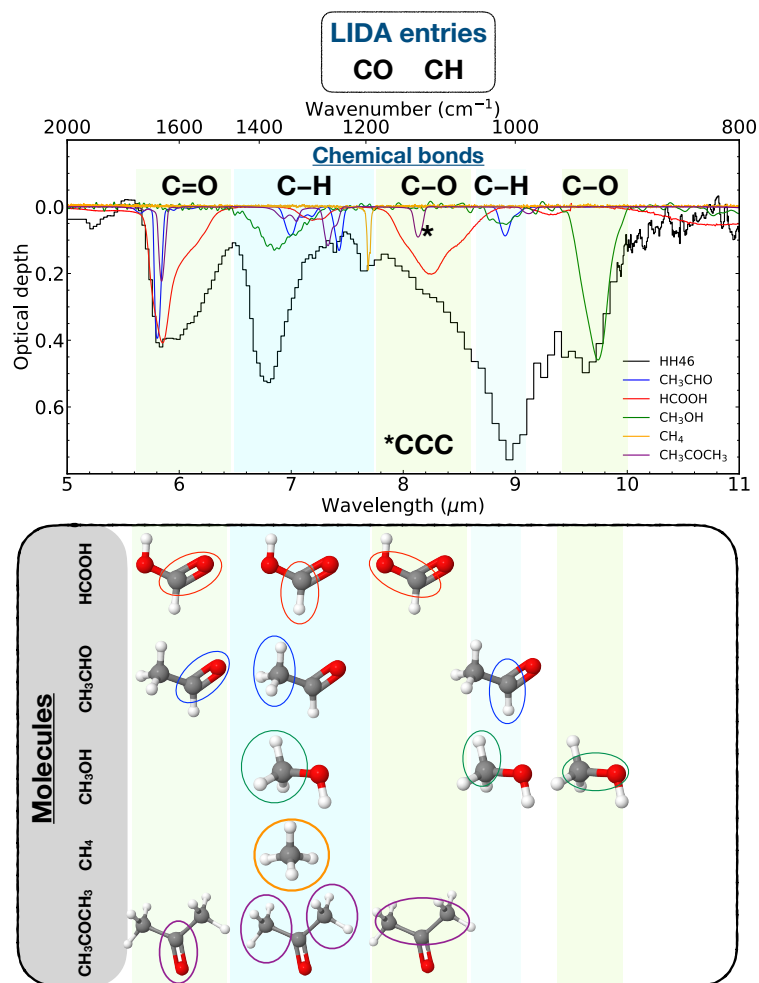
Fig. 8. Illustration on how to use LIDA to interpret astronomical observations. *Top*: LIDA entries to search for molecules sharing CO and CH chemical bonds. *Middle*: selected experimental data scaled to the water-silicate-subtracted spectra of the protostar HH46. *Bottom*: molecules representing the pure ices used to match the HH46 spectrum. The ellipses indicate which part of a molecule is responsible for a specific absorption band, and the colors follow the same color-code used in the middle panel.

contribution of different functional groups and chemical bonds to the overall absorption profile of features observed in interstellar ice spectra. It should be noted that such synthetic spectra allow the reproduction of observed data but do not necessarily provide a unique solution. Other public codes, such as the `ENIIGMA` fitting tool (Rocha et al. 2021) have the goal of quantifying the degeneracy of those fits when a large dataset of inputs is taken into account.

4.2. Infrared refractive index calculator

In this section, we introduce the refractive index online calculator, which is publicly available through LIDA. The web interface

of this tool is shown in Fig. C.3. This tool uses the approach adopted in Rocha & Pilling (2014) for the `NKABS` code and is briefly described below.

The goal of the tool is to calculate the real (n) and imaginary (k) parts of CRI ($\tilde{m}$) from the absorbance spectrum (Eq. (2)) of the ice sample as a function of the wave number (ν, in units of cm^{-1}). The input experimental data is the absorbance spectrum given in `ascii` format. Other input parameters are required before starting the calculation. They are the thickness of the ice sample (d) in µm, the refractive index of the sample around 670 nm (n_0) or at the wavelength of the HeNe laser used in the experiments, the real refractive index of the substrate, and the mean average percentage error (MAPE) that is used as a stop criterion.

Table 6. Input parameters used to calculate the mid-IR water ice CRI.

Parameters	Values	Reference
Thickness [a] (cm)	1.0×10^{-4}	Öberg et al. (2007)
$n_0^{30\,K}$	1.16	He et al. (2022)
$n_0^{75\,K}$	1.21	He et al. (2022)
$n_0^{105\,K}$	1.23	He et al. (2022)
$n_0^{135\,K}$	1.25	He et al. (2022)
$n_{substrate}$	1.73	Querry (1987)
Initial MAPE	0.1%	...
After calculation		
Final MAPE	$\leq 0.03\%$	...
Iterations	5	...

Notes. [a] Assuming 1 ML ~3.4 Å (González Díaz et al. 2019).

Equations (9) and (10) are solved interactively, and new values of k are used to calculate new values of n. Subsequently, new n improves k, until the convergence criteria is reached. The numerical implementation of these equations is described in Rocha & Pilling (2014) and follows the procedure presented in Ohta & Ishida (1988) to solve the Kramers-Kronig equation. As an example, we calculate the CRI values of pure H_2O at 30, 75, 105, and 135 K. The H_2O ice IR spectra used as input are taken from Öberg et al. (2007), namely, `Pure H2O (3000 ML)`[24]. Table 6 lists the n_0 values, the number of iterations used by the tool, and the final MAPE.

The data from OASIS and from the theoretical calculation cover two spectral ranges, that is 0.25–0.7 μm and 2–20 μm, respectively. The interval between 0.7 and 2 μm is not available in the experimental spectrum. We deal with this missing data using different approaches to determine n and k. For k values, we extrapolate the imaginary refractive index at 2 μm (10^{-4}) until 0.25 μm. In the case of n, we use a low-order polynomial to link the water ice n values from He et al. (2022) to the data starting at 2 μm. The caveat in this approach is that we do not take into account the water ice absorption bands in the interval between 0.7 and 2 μm. However, the absorption features between 1.4 and 1.8 μm for amorphous and crystalline water ice are very weak (Mastrapa et al. 2008). For example, the k values calculated by Mastrapa et al. (2008) range from 10^{-5} to 10^{-3}, which is close to the value used in our extrapolation (10^{-4}). Similarly, the variation in n is 0.2% between the lowest and highest values.

The results are visualized in the "refractive index viewer" shown in Fig. 9 for the data at 30 K. A download of the data files and plots is also available. A terminal-based version of this tool is available for download in the GitHub[25] repository of LIDA. Both Linux and executable files for Windows platforms can be used for highly resolved spectral data that demand high computational efficiency.

5. Future upgrades

LIDA already has relevant data for all molecules securely or tentatively detected toward protostars (e.g., Tables 1 and A.1) and covers the most abundant species for the JWST, but more data are necessary to further boost the interpretation of upcoming observations. Table 7 lists the molecules that are missing
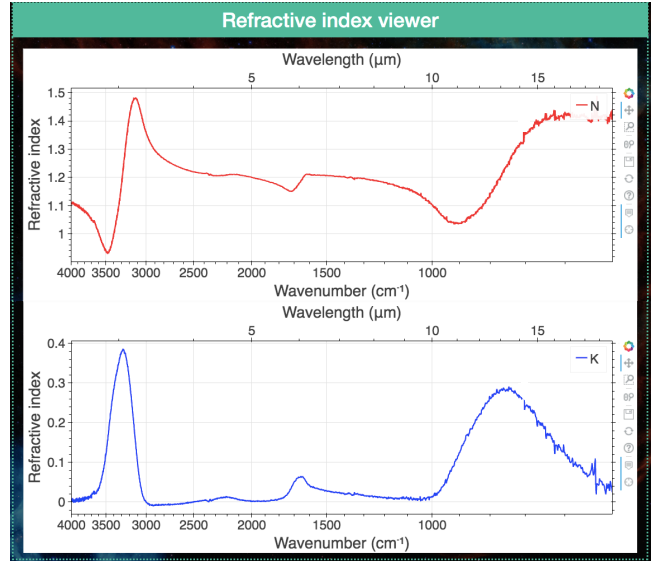
Fig. 9. Screenshot of refractive index viewer showing wavelength-dependent CRI of H_2O ice at 30 K. The *top and bottom panels* show the real and imaginary refractive index values, respectively.

Table 7. List of missing molecules in LIDA, which will be included via new measurements or data sharing from other laboratories.

Molecule	Name
<6 atoms	
C_2H_2	Acetylene
H_2S	Hydrogen sulfide
HNCO	Isocyanic acid
HCN	Hydrogen cyanide
NH_2OH	Hydroxylamine
≥6 atoms	
NH_2CHO	Formamide
H_2CO_3	Carbonic acid
$HOCH_2CHO$	Glycolaldehyde

in the current version of LIDA but are being measured or will be targeted in future experiments. Similarly, temperature- and wavelength-dependent refractive index values of CO, CO_2, NH_3, and CH_3OH were recently measured on the OASIS setup and will be added to the database after data reduction (Rachid et al. in prep.). We also mention that LIDA is available to host data from other astrochemistry groups. Here, we hope that having one central point from which to search for ice properties will be considered helpful for the whole ice community.

The online tools will also be further developed to support astronomical data interpretation. With this goal in mind, the effect of grain shape will be available when simulating synthetic spectra of protostars. Additionally, the UV/vis n and k values of different ices and ice mixtures will be included in LIDA. Another forthcoming LIDA upgrade is the inclusion of diagnostic plots relating the peak position and full width at half maximum (FWHM) of ice features that can be compared with similar information from different astronomical observations.

6. Summary and outlook

The Leiden Ice Database has served the astronomical community for more than 20 yr by providing IR spectra of ice samples.

In 2015, all ice IR spectra were combined on one server and visualization tools were developed. In this paper, we present the most recent version of LIDA, which includes over 1100 IR spectra of ice samples in astrophysically relevant conditions, as well as the UV/vis and mid-IR refractive indices of H_2O at different temperatures. In addition to the wide range of experimental data, the current upgrade includes astronomy-oriented online tools to help the interpretation of observations provided by the JWST, in general, as well as the past ice observations. Both data and tools are provided in a user-friendly format to boost the usability of the database. It is worth mentioning that LIDA is a specific deliverable within ICE AGE, an ERS JWST program.

The database is under expansion, and spectra of several COMs and refractive index values of other ices will become publicly available in the next months and years. It is also hoped that other laboratory groups will make their ice spectra available through LIDA. Also, the online tools in the database will be further developed to meet to the need to interpret ice observations in the upcoming years with the JWST, the METIS (Mid-Infrared Extremely Large Telescope Imager and Spectrograph) on the Extremely Large Telescope (ELT), and the SPHEREx (Spectro-Photometer for the History of the Universe, Epoch of Reionization and Ices Explorer). More information about LIDA can be found in the public-access online documentation[26].

References

Balkanski, M. 1989, Infrared Phys., 29, 729
Baratta, G. A., & Palumbo, M. E. 1998, J. Opt. Soc. Am. A, 15, 3076
Bauschlicher, C. W., J., Boersma, C., Ricca, A., et al. 2010, ApJS, 189, 341
Becke, A. D. 1993, J. Chem. Phys., 98, 5648
Belloche, A., Maury, A. J., Maret, S., et al. 2020, A&A, 635, A198
Beltrán, M. D., Molina, R. L., Aznar, M. Á. S., Moltó, C. S., & Verdú, C. M. 2015, Sensors, 15, 25123
Bernstein, M. P., Sandford, S. A., Allamandola, L. J., Chang, S., & Scharberg, M. A. 1995, ApJ, 454, 327
Bisschop, S. E., Fuchs, G. W., Boogert, A. C. A., van Dishoeck, E. F., & Linnartz, H. 2007, A&A, 470, 749
Blake, G. A., Sutton, E. C., Masson, C. R., & Phillips, T. G. 1987, ApJ, 315, 621
Boersma, C., Bauschlicher, C. W., J., Ricca, A., et al. 2014, ApJS, 211, 8
Bokeh Development Team 2018, Bokeh: Python library for interactive visualization
Bolton, E. E., Chen, J., Kim, S., et al. 2011, J. Cheminformatics, 3, 1
Boogert, A. C. A., Schutte, W. A., Helmich, F. P., Tielens, A. G. G. M., & Wooden, D. H. 1997, A&A, 317, 929
Boogert, A. C. A., Tielens, A. G. G. M., Ceccarelli, C., et al. 2000, A&A, 360, 683
Boogert, A. C. A., Blake, G. A., & Tielens, A. G. G. M. 2002a, ApJ, 577, 271
Boogert, A. C. A., Hogerheijde, M. R., Ceccarelli, C., et al. 2002b, ApJ, 570, 708
Boogert, A. C. A., Pontoppidan, K. M., Knez, C., et al. 2008, ApJ, 678, 985
Boogert, A. C. A., Chiar, J. E., Knez, C., et al. 2013, ApJ, 777, 73
Boogert, A. C. A., Gerakines, P. A., & Whittet, D. C. B. 2015, ARA&A, 53, 541
Bossa, J. B., Isokoski, K., Paardekooper, D. M., et al. 2014, A&A, 561, A136
Bossa, J.-B., Maté, B., Fransen, C., et al. 2015, ApJ, 814, 47
Bottinelli, S., Boogert, A. C. A., Bouwman, J., et al. 2010, ApJ, 718, 1100
Boudin, N., Schutte, W. A., & Greenberg, J. M. 1998, A&A, 331, 749
Bouilloud, M., Fray, N., Bénilan, Y., et al. 2015, MNRAS, 451, 2145
Bouwman, J., Ludwig, W., Awad, Z., et al. 2007, A&A, 476, 995
Brown, W. L., Lanzerotti, L. J., & Johnson, R. E. 1982, Science, 218, 525
Bruggeman, D. A. G. 1935, Ann. Phys., 416, 665
Bruggeman, D. A. G. 1936, Ann. Phys., 417, 645
Brunken, N. G. C., Booth, A. S., Leemker, M., et al. 2022, A&A, 659, A29
Bulak, M., Paardekooper, D. M., Fedoseev, G., & Linnartz, H. 2021, A&A, 647, A82
Ciaravella, A., Jiménez-Escobar, A., Cecchi-Pestellini, C., et al. 2019, ApJ, 879, 21
Clark, R. N., Cruikshank, D. P., Jaumann, R., et al. 2012, Icarus, 218, 831
Coblentz, W. W. 1905, Phys. Rev. (Series I), 20, 337
Cuppen, H. M., Penteado, E. M., Isokoski, K., van der Marel, N., & Linnartz, H. 2011, MNRAS, 417, 2809
D'Alessio, P., Calvet, N., Hartmann, L., Franco-Hernández, R., & Servín, H. 2006, ApJ, 638, 314
Dalle Ore, C. M., Cruikshank, D. P., Mastrapa, R. M. E., Lewis, E., & White, O. L. 2015, Icarus, 261, 80
Danger, G., Borget, F., Chomat, M., et al. 2011, A&A, 535, A47
Dartois, E., & d'Hendecourt, L. 2001, A&A, 365, 144
Dartois, E., d'Hendecourt, L., Thi, W., Pontoppidan, K. M., & van Dishoeck, E. F. 2002, A&A, 394, 1057
Dartois, E., Noble, J. A., Ysard, N., Demyk, K., & Chabot, M. 2022, A&A, 666, A153
de Graauw, T., Whittet, D. C. B., Gerakines, P. A., et al. 1996, A&A, 315, L345
D'Hendecourt, L. B., & Allamandola, L. J. 1986, A&As, 64, 453
Domaracka, A., Seperuelo Duarte, E., Boduch, P., et al. 2010, Nucl. Instrum. Methods Phys. Res. B, 268, 2960
Dominik, C., Min, M., & Tazaki, R. 2021, OpTool: Command-line driven tool for creating complex dust opacities
Dubernet, M.-L., Grosjean, A., Flower, D., et al. 2006, J. Plasma Res. Ser., 7, 356
Dubernet, M. L., Alexander, M. H., Ba, Y. A., et al. 2013, A&A, 553, A50
Ehrenfreund, P., Boogert, A. C. A., Gerakines, P. A., et al. 1996, A&A, 315, L341
Ehrenfreund, P., Boogert, A. C. A., Gerakines, P. A., Tielens, A. G. G. M., & van Dishoeck, E. F. 1997, A&A, 328, 649
Ehrenfreund, P., Kerkhof, O., Schutte, W. A., et al. 1999, A&A, 350, 240
Endres, C. P., Schlemmer, S., Schilke, P., Stutzki, J., & Müller, H. S. P. 2016, J. Mol. Spectrosc., 327, 95
Fayolle, E. C., Öberg, K. I., Cuppen, H. M., Visser, R., & Linnartz, H. 2011, A&A, 529, A74
Fedoseev, G., Chuang, K. J., Ioppolo, S., et al. 2017, ApJ, 842, 52
Fraser, H. J., & van Dishoeck, E. F. 2004, Adv. Space Res., 33, 14
Fuchs, G. W., Acharyya, K., Bisschop, S. E., et al. 2006, Faraday Discuss., 133, 331
Fuchs, G. W., Cuppen, H. M., Ioppolo, S., et al. 2009, A&A, 505, 629
Garnett, J. C. M. 1904, Philos. Trans. Roy. Soc. Lond. Ser. A, 203, 385
Garnett, J. C. M. 1906, Philos. Trans. Roy. Soc. Lond. Ser. A, 205, 237
Gerakines, P. A., & Hudson, R. L. 2020, ApJ, 901, 52
Gerakines, P. A., Schutte, W. A., Greenberg, J. M., & van Dishoeck, E. F. 1995, A&A, 296, 810
Gerakines, P. A., Schutte, W. A., & Ehrenfreund, P. 1996, A&A, 312, 289
Gibb, E. L., & Whittet, D. C. B. 2002, ApJ, 566, L113
Gibb, E. L., Whittet, D. C. B., Boogert, A. C. A., & Tielens, A. G. G. M. 2004, ApJS, 151, 35
Gillett, F. C., & Forrest, W. J. 1973, ApJ, 179, 483
Glasse, A., Rieke, G. H., Bauwens, E., et al. 2015, PASP, 127, 686
González Díaz, C., Carrascosa de Lucas, H., Aparicio, S., et al. 2019, MNRAS, 486, 5519
Grim, R. J. A., Greenberg, J. M., de Groot, M. S., et al. 1989, A&AS, 78, 161
Grinberg, M. 2018, Flask Web Development: Developing Web Applications with Python (O'Reilly Media, Inc.)
Hagen, W., Allamandola, L. J., & Greenberg, J. M. 1979, Ap&SS, 65, 215
He, J., Diamant, S. J., Wang, S., et al. 2022, ApJ, 925, 179
Heays, A. N., Bosman, A. D., & van Dishoeck, E. F. 2017, A&A, 602, A105
Henning, T., Il'In, V. B., Krivova, N. A., Michel, B., & Voshchinnikov, N. V. 1999, A&As, 136, 405
Herbst, E., & van Dishoeck, E. F. 2009, ARA&A, 47, 427
Hudgins, D. M., Sandford, S. A., Allamandola, L. J., & Tielens, A. G. G. M. 1993, ApJS, 86, 713
Hudson, R. L. 2017, Spectrochim. Acta A: Mol. Spectrosc., 187, 82
Hudson, R. L., Moore, M. H., & Gerakines, P. A. 2001, ApJ, 550, 1140
Hudson, R. L., Loeffler, M. J., & Gerakines, P. A. 2017, J. Chem. Phys., 146, 024304

---

[26] https://leiden-ice-database.readthedocs.io

Hudson, R. L., Gerakines, P. A., & Ferrante, R. F. 2018, Spectrochim. Acta A: Mol. Spectrosc., 193, 33

Ioppolo, S., Fedoseev, G., Chuang, K. J., et al. 2021, Nat. Astron., 5, 197

Ishibashi, A., Hidaka, H., Oba, Y., Kouchi, A., & Watanabe, N. 2021, ApJ, 921, L13

Isokoski, K., Poteet, C. A., & Linnartz, H. 2013, A&A, 555, A85

Jäger, C., Il'in, V. B., Henning, T., et al. 2003, J. Quant. Spec. Radiat. Transf., 79–80, 765

Jmol development team: Accessed in June 2021, Jmol: an open-source Java viewer for chemical structures in 3D

Jørgensen, J. K., Favre, C., Bisschop, S. E., et al. 2012, ApJ, 757, L4

Jørgensen, J. K., Belloche, A., & Garrod, R. T. 2020, ARA&A, 58, 727

Keane, J. V., Tielens, A. G. G. M., Boogert, A. C. A., Schutte, W. A., & Whittet, D. C. B. 2001, A&A, 376, 254

Kemper, F., Vriend, W. J., & Tielens, A. G. G. M. 2004, ApJ, 609, 826

Kerkhof, O., Schutte, W. A., & Ehrenfreund, P. 1999, A&A, 346, 990

Kim, S., Chen, J., Cheng, T., et al. 2020, Nucleic Acids Res., 49, D1388

Knez, C., Moore, M. H., Ferrante, R. F., & Hudson, R. L. 2012, ApJ, 748, 95

Kofman, V., He, J., ten Kate, I. L., & Linnartz, H. 2019, ApJ, 875, 131

Kramers, H. A. 1927, Atti Cong. Intern. Fisica (Trans. Volta Centenary Congress) Como, 2, 545

Kronig, R. D. L. 1926, J. Opt. Soc. Am., 12, 547

Lacy, J. H., Baas, F., Allamandola, L. J., et al. 1984, ApJ, 276, 533

Lacy, J. H., Carr, J. S., Evans, Neal J., I., et al. 1991, ApJ, 376, 556

Lacy, J. H., Faraji, H., Sandford, S. A., & Allamandola, L. J. 1998, ApJ, 501, L105

Langmuir, I. 1938, Science, 87, 493

Ligterink, N. F. W., Walsh, C., Bhuin, R. G., et al. 2018, A&A, 612, A88

Linnartz, H., Ioppolo, S., & Fedoseev, G. 2015, Int. Rev. Phys. Chem., 34, 205

Mastrapa, R. M., Bernstein, M. P., Sandford, S. A., et al. 2008, Icarus, 197, 307

Mastrapa, R. M., Sandford, S. A., Roush, T. L., Cruikshank, D. P., & Dalle Ore, C. M. 2009, ApJ, 701, 1347

Maté, B., Gálvez, O., Herrero, V. J., et al. 2009, ApJ, 703, L178

Maté, B., Herrero, V. J., Rodríguez-Lazcano, Y., et al. 2012, ApJ, 759, 90

Materese, C. K., Cruikshank, D. P., Sandford, S. A., Imanaka, H., & Nuevo, M. 2015, ApJ, 812, 150

Mattioda, A. L., Hudgins, D. M., Boersma, C., et al. 2020, ApJS, 251, 22

McElroy, D., Walsh, C., Markwick, A. J., et al. 2013, A&A, 550, A36

McGuire, B. A. 2022, ApJS, 259, 30

McGuire, B. A., Carroll, P. B., Loomis, R. A., et al. 2016, Science, 352, 1449

McLean, I. S., Becklin, E. E., Bendiksen, O., et al. 1998, SPIE Conf. Ser., 3354, 566

Meinert, C., Myrgorodska, I., de Marcellus, P., et al. 2016, Science, 352, 208

Merrill, K. M., Russell, R. W., & Soifer, B. T. 1976, ApJ, 207, 763

Mifsud, D. V., Juhász, Z., Herczku, P., et al. 2021, Eur. Phys. J. D, 75, 182

Modica, P., & Palumbo, M. E. 2010, A&A, 519, A22

Moore, M. H., Ferrante, R. F., Moore, W. J., & Hudson, R. 2010, ApJS, 191, 96

Muñoz Caro, G. M., & Schutte, W. A. 2003, A&A, 412, 121

Muñoz Caro, G. M., Meierhenrich, U. J., Schutte, W. A., et al. 2002, Nature, 416, 403

Müller, H. S. P., Thorwirth, S., Roth, D. A., & Winnewisser, G. 2001, A&A, 370, L49

Müller, H. S. P., Schlöder, F., Stutzki, J., & Winnewisser, G. 2005, J. Mol. Struct., 742, 215

Nazari, P., van Gelder, M. L., van Dishoeck, E. F., et al. 2021, A&A, 650, A150

Neese, F. 2012, WIREs Comput. Mol. Sci., 2, 73

Neese, F. 2018, WIREs Comput. Mol. Sci., 8, e1327

Neese, F., Wennmohs, F., Becker, U., & Riplinger, C. 2020, J. Chem. Phys., 152, 224108

Novozamsky, J. H., Schutte, W. A., & Keane, J. V. 2001, A&A, 379, 588

Nuevo, M., Cooper, G., & Sandford, S. A. 2018, Nat. Commun., 9, 5276

Öberg, K. I. 2016, Chem. Rev., 116, 9631

Öberg, K. I., Fraser, H. J., Boogert, A. C. A., et al. 2007, A&A, 462, 1187

Öberg, K. I., Garrod, R. T., van Dishoeck, E. F., & Linnartz, H. 2009, A&A, 504, 891

Öberg, K. I., Boogert, A. C. A., Pontoppidan, K. M., et al. 2011, ApJ, 740, 109

Ohta, K., & Ishida, H. 1988, Appl. Spectrosc., 42, 952

Onaka, T., Kimura, T., Sakon, I., & Shimonishi, T. 2021, ApJ, 916, 75

Palumbo, M. E. 2006, A&A, 453, 903

Palumbo, M. E., Tielens, A. G. G. M., & Tokunaga, A. T. 1995, ApJ, 449, 674

Palumbo, M. E., Baratta, G. A., Brucato, J. R., et al. 1998, A&A, 334, 247

Palumbo, M. E., Baratta, G. A., Collings, M. P., & McCoustra, M. R. S. 2006, Phys. Chem. Chem. Phys. (Incorp. Faraday Trans.), 8, 279

Pearson, J. C., Müller, H. S. P., Pickett, H. M., Cohen, E. A., & Drouin, B. J. 2010, J. Quant. Spec. Radiat. Transf., 111, 1614

Penteado, E. M., Boogert, A. C. A., Pontoppidan, K. M., et al. 2015, MNRAS, 454, 531

Perotti, G., Rocha, W. R. M., Jørgensen, J. K., et al. 2020, A&A, 643, A48

Pickett, H. M., Poynter, R. L., Cohen, E. A., et al. 1998, J. Quant. Spec. Radiat. Transf., 60, 883

Pilling, S., & Bergantini, A. 2015, ApJ, 811, 151

Pilling, S., Seperuelo Duarte, E., Domaracka, A., et al. 2010, A&A, 523, A77

Pontoppidan, K. M., Fraser, H. J., Dartois, E., et al. 2003, A&A, 408, 981

Pontoppidan, K. M., Dullemond, C. P., van Dishoeck, E. F., et al. 2005, ApJ, 622, 463

Pontoppidan, K. M., Boogert, A. C. A., Fraser, H. J., et al. 2008, ApJ, 678, 1005

Pontoppidan, K. M., Pickering, T. E., Laidler, V. G., et al. 2016, SPIE Conf. Ser., 9910, 991016

Potapov, A., Bouwman, J., Jäger, C., & Henning, T. 2021, Nat. Astron., 5, 78

Poteet, C. A., Pontoppidan, K. M., Megeath, S. T., et al. 2013, ApJ, 766, 117

Querry, M. R. 1987, in Optical constants of minerals and other materials from the millimeter to the ultraviolet

Rachid, M. G., Terwisscha van Scheltinga, J., Koletzki, D., & Linnartz, H. 2020, A&A, 639, A4

Rachid, M. G., Brunken, N., de Boe, D., et al. 2021, A&A, 653, A116

Rachid, M. G., Rocha, W., & Linnartz, H. 2022, A&A 665, A89

Rivilla, V. M., Jiménez-Serra, I., Martín-Pintado, J., et al. 2021, Proc. Natl. Acad. Sci. U.S.A., 118, 2101314118

Rocha, W., & Pilling, S. 2014, Spectroch. Acta A: Mol. Biomol. Spectrosc., 123, 436

Rocha, W. R. M., & Pilling, S. 2015, ApJ, 803, 18

Rocha, W. R. M., & Pilling, S. 2018, MNRAS, 478, 5190

Rocha, W. R. M., Pilling, S., Domaracka, A., Rothard, H., & Boduch, P. 2020, Spectrochim. Acta A: Mol. Spectrosc., 228, 117826

Rocha, W. R. M., Perotti, G., Kristensen, L. E., & Jørgensen, J. K. 2021, A&A, 654, A158

Schmitt, B., Grim, R., & Greenberg, M. 1989, in Infrared Spectroscopy in Astronomy, ed. E. Böhm-Vitense, 213

Schmitt, B., Bollard, P., Garenne, A., et al. 2018, in European Planetary Science Congress, EPSC2018-529

Schöier, F. L., van der Tak, F. F. S., van Dishoeck, E. F., & Black, J. H. 2005, A&A, 432, 369

Schutte, W. A. 1999, in NATO Advanced Study Institute (ASI) Series C, Vol. 523, Formation and Evolution of Solids in Space, eds. J. M. Greenberg & A. Li, 177

Schutte, W. A., & Greenberg, J. M. 1997, A&A, 317, L43

Schutte, W. A., & Khanna, R. K. 2003, A&A, 398, 1049

Schutte, W. A., Tielens, A. G. G. M., Whittet, D. C. B., et al. 1996, A&A, 315, L333

Schutte, W. A., Boogert, A. C. A., Tielens, A. G. G. M., et al. 1999, A&A, 343, 966

Smith, R. G., Sellgren, K., & Tokunaga, A. T. 1989, ApJ, 344, 413

Stephens, P. J., Devlin, F. J., Chabalowski, C. F., & Frisch, M. J. 1994, J. Phys. Chem., 98, 11623

Strazzulla, G., Cataliotti, R. S., Calcagno, L., & Foti, G. 1984, A&A, 133, 77

Tempelmeyer, K., & Mills Jr, D. 1968, J. Appl. Phys., 39, 2968

Terwisscha van Scheltinga, J., Ligterink, N. F. W., Boogert, A. C. A., van Dishoeck, E. F., & Linnartz, H. 2018, A&A, 611, A35

Terwisscha van Scheltinga, J., Marcandalli, G., McClure, M. K., Hogerheijde, M. R., & Linnartz, H. 2021, A&A, 651, A95

Theulé, P., Duvernay, F., Danger, G., et al. 2013, Adv. Space Res., 52, 1567

Urso, R. G., Vuitton, V., Danger, G., et al. 2020, A&A, 644, A115

van Broekhuizen, F. A. 2005, PhD thesis, Leiden Observatory, Leiden University, The Netherlands

van Broekhuizen, F. A., Pontoppidan, K. M., Fraser, H. J., & van Dishoeck, E. F. 2005, A&A, 441, 249

van Broekhuizen, F. A., Groot, I. M. N., Fraser, H. J., van Dishoeck, E. F., & Schlemmer, S. 2006, A&A, 451, 723

van der Tak, F. F. S., Lique, F., Faure, A., Black, J. H., & van Dishoeck, E. F. 2020, Atoms, 8, 15

van Dishoeck, E. F. 1988, in Astrophysics and Space Science Library, 146, Rate Coefficients in Astrochemistry, eds. T. J. Millar & D. A. Williams, 49

van Dishoeck, E. F., Jonkheid, B., & van Hemert, M. C. 2006, Faraday Discuss., 133, 231

van Gelder, M. L., Tabone, B., Tychoniec, Ł., et al. 2020, A&A, 639, A87

Vinogradoff, V., Duvernay, F., Fray, N., et al. 2015, ApJ, 809, L18

Wakelam, V., Herbst, E., Loison, J. C., et al. 2012, ApJS, 199, 21

Warren, S. G. 1984, Appl. Opt., 23, 1206

Watanabe, N., & Kouchi, A. 2002, ApJ, 571, L173

Weingartner, J. C., & Draine, B. T. 2001, ApJ, 548, 296

Zasowski, G., Kemper, F., Watson, D. M., et al. 2009, ApJ, 694, 459

Appendix A: List of ice samples in LIDA

The current version of LIDA contains the IR spectrum of over 1100 ice samples, which are listed in Table A.1. They are categorized by ices in pure samples, and mixtures with, two, three, four, and five components. This also includes warmed-up samples or those processed by UV radiation.

Table A.1. Ice analogues hosted in LIDA. Irradiated samples are indicated by the symbol $\leadsto$. "s" and "h" indicate seconds and hour, respectively.

Sample	Thickness (ML)	$N_{ice}{}^a$ (cm^{-2})	Resolution (cm^{-1})	Ratios	Temperature (K)/ UV radiation (time)	Substrate/ $n_{substrate}$	Reference
				Pure ices			
H_2O	500	5e17	1.0	...	10–160	CsI/1.73	Gerakines et al. (1996)
H_2O	3000	1e17	2.0	...	15–135	CsI/1.73	Öberg et al. (2007)
H_2O	10000	3.5e17	2.0	...	15–135	CsI/1.73	Öberg et al. (2007)
H_2O ($\leadsto$)	500	4.4e17	1.0	...	10/5s–1h	CsI/1.73	Gerakines et al. (1996)
H_2O ($\leadsto$)	500	4.4e17	1.0	...	25–160/1h	CsI/1.73	Gerakines et al. (1996)
CO	600	6e17	0.5	...	15–45	CsI/1.73	van Broekhuizen et al. (2006)
CO ($\leadsto$)	500	5e17	1.0	...	10/5s–1h	CsI/1.73	Gerakines et al. (1996)
CO ($\leadsto$)	500	5e17	1.0	...	26–105/1h	CsI/1.73	Gerakines et al. (1996)
CO_2	600	6e17	0.5	...	15–130	CsI/1.73	van Broekhuizen et al. (2006)
CO_2 ($\leadsto$)	500	5e17	1.0	...	10/5s–1h	CsI/1.73	Gerakines et al. (1996)
CO_2 ($\leadsto$)	500	5e17	1.0	...	30,70/1h	CsI/1.73	Gerakines et al. (1996)
CH_4 ($\leadsto$)	500	5e17	1.0	...	10/5s–1h	CsI/1.73	Gerakines et al. (1996)
CH_4 ($\leadsto$)	500	5e17	1.0	...	25–280/1h	CsI/1.73	Gerakines et al. (1996)
NH_3	500	5e17	1.0	...	10	CsI/1.73	Gerakines et al. (1996)
NH_3 ($\leadsto$)	500	5e17	1.0	...	25–280/1h	CsI/1.73	Gerakines et al. (1996)
NH_3 ($\leadsto$)	500	5e17	1.0	...	27,60/5s–1h	CsI/1.73	Gerakines et al. (1996)
SO_2	4000	4.5e17	1.0	...	10	CsI/1.73	Boogert et al. (1997)
H_2CO	500	3.7e18	1.0	...	10	CsI/1.73	Gerakines et al. (1996)
H_2CO ($\leadsto$)	500	5.1e17	1.0	...	10/5s–1h	CsI/1.73	Gerakines et al. (1996)
H_2CO ($\leadsto$)	500	1.1e17	1.0	...	30–275/1h	CsI/1.73	Gerakines et al. (1996)
NH_4^+	<500	3e18	1.0	...	80	CsI/1.73	Novozamsky et al. (2001)
OCN^-	<500	<5e17	1.0	...	80	CsI/1.73	Novozamsky et al. (2001)
OCS	620	6.2e17	0.9	...	10–170	KBr/1.54	Rachid et al. (in prep.)
CH_3OH	3400	3.4e18	0.5	...	15	ZnSe/2.54	Terwisscha van Scheltinga et al. (2018)
CH_3OH	4000	6.1e16	0.5	...	15–160	...	Fraser & van Dishoeck (2004)
CH_3OH ($\leadsto$)	500	5e17	1.0	...	10/5s–1h	CsI/1.73	Gerakines et al. (1996)
CH_3OH ($\leadsto$)	500	5e17	1.0	...	25–230/1h	CsI/1.73	Gerakines et al. (1996)
$HCOOH$	900	1.4e17	1.0	...	30–105	CsI/1.73	Bisschop et al. (2007)
$HCOOH$	900	1.4e17	1.0	...	145 (deposition)	CsI/1.73	Bisschop et al. (2007)
CH_3CHO	4500	9.7e18	1.0	...	30–120	ZnSe/2.54	Terwisscha van Scheltinga et al. (2018)
CH_3OCH_3	4500	2.9e18	1.0	...	30–100	ZnSe/2.54	Terwisscha van Scheltinga et al. (2018)
CH_3CH_2OH	4500	3e18	1.0	...	30–150	ZnSe/2.54	Terwisscha van Scheltinga et al. (2018)
CH_3COCH_3	2800	2.1e18	0.5	...	15–140	ZnSe/2.54	Rachid et al. (2020)
CH_3OCHO	2000	2.2e18	0.5	...	15–120	ZnSe/2.54	Terwisscha van Scheltinga et al. (2021)
CH_3NH_2	850	1.6e18	0.5	...	15–140	ZnSe/2.54	Rachid et al. (2021)
CH_3CN	5000	3.0e18	1.0	...	15–150	KBr/1.54	Rachid et al. (2022)
				Binary mixtures			
H_2O:CO	2500	5.1e17	1.0	1:100	15,30	CsI/1.73	Ehrenfreund et al. (1997)
H_2O:CO	2500	4.2e17	1.0	100:14	10	CsI/1.73	Ehrenfreund et al. (1997)
CO:OCS	...	...	0.9	20:1	11,20	KBr/1.54	Rachid et al. (in prep.)
CO_2:OCS	...	...	0.9	24:1	11–70	KBr/1.54	Rachid et al. (in prep.)
H_2O:OCS	...	...	0.9	20:1	11–120	KBr/1.54	Rachid et al. (in prep.)

Table A.1. Continued.

Sample	Thickness (ML)	$N_{\rm ice}$[a] (cm^{-2})	Resolution (cm^{-1})	Ratios	Temperature (K)/ UV radiation (time)	Substrate/ $n_{\rm substrate}$	Reference
$CO:O_2$	2500	1.2×10^{17}	1.0	100:50	10,35	CsI/1.73	Ehrenfreund et al. (1997)
$CO:O_2$	2500	1×10^{17}	1.0	100:70	10	CsI/1.73	Ehrenfreund et al. (1997)
$H_2O:CO_2$	2500	3.9×10^{17}	1.0	1:100	10,30	CsI/1.73	Ehrenfreund et al. (1997)
$H_2O:CO_2$	2500	1.7×10^{17}	1.0	1:10	10,80	CsI/1.73	Ehrenfreund et al. (1997)
$H_2O:CO_2$	2500	1.2×10^{17}	1.0	1:6	10–75	CsI/1.73	Ehrenfreund et al. (1997)
$H_2O:CO_2$	2500	4.6×10^{17}	1.0	100:14	10	CsI/1.73	Ehrenfreund et al. (1997)
$CO:CO_2$	2500	2×10^{17}	1.0	100:4	10,30	CsI/1.73	Ehrenfreund et al. (1997)
$CO:CO_2$	2500	1.5×10^{17}	1.0	100:8	10,30	CsI/1.73	Ehrenfreund et al. (1997)
$CO:CO_2$	2500	1.4×10^{17}	1.0	100:16	10,30	CsI/1.73	Ehrenfreund et al. (1997)
$CO:CO_2$	2500	1.4×10^{17}	1.0	100:21	10,30	CsI/1.73	Ehrenfreund et al. (1997)
$CO:CO_2$	2500	1×10^{17}	1.0	100:23	10,30	CsI/1.73	Ehrenfreund et al. (1997)
$CO:CO_2$	2500	1.3×10^{17}	1.0	100:26	10,30	CsI/1.73	Ehrenfreund et al. (1997)
$CO_2:O_2$	2500	1×10^{17}	1.0	1:1	10	CsI/1.73	Ehrenfreund et al. (1997)
$HCOOH:CH_3OH$	1800	8.3×10^{17}	1.0	1:9	15–75	CsI/1.73	Bisschop et al. (2007)
$HCOOH:CO$	1800	1.25×10^{18}	1.0	1:9	15–165	CsI/1.73	Bisschop et al. (2007)
$HCOOH:H_2O$	900	5.5×10^{17}	1.0	0.25:1	15–165	CsI/1.73	Bisschop et al. (2007)
$HCOOH:H_2O$	900	3.7×10^{17}	1.0	0.5:1	15–165	CsI/1.73	Bisschop et al. (2007)
$HCOOH:H_2O$	900	5.5×10^{17}	1.0	1:1	15–165	CsI/1.73	Bisschop et al. (2007)
$HCOOH:H_2O$	900	6×10^{17}	1.0	0.1:1	15–165	CsI/1.73	Bisschop et al. (2007)
$HCOOH:CO_2$	900	6×10^{17}	1.0	0.1:1	15–165	CsI/1.73	Bisschop et al. (2007)
$H_2O:C^{18}O_2$	2000	1.1×10^{17}	2.0	1:1	15–135	CsI/1.73	Öberg et al. (2007)
$H_2O:C^{18}O_2$	6000	1.95×10^{17}	2.0	1:1	15–135	CsI/1.73	Öberg et al. (2007)
$H_2O:C^{18}O_2$	20000	6.2×10^{17}	2.0	1:1	15–135	CsI/1.73	Öberg et al. (2007)
$H_2O:C^{18}O_2$	9000	1.3×10^{17}	2.0	1:2	15–135	CsI/1.73	Öberg et al. (2007)
$H_2O:C^{18}O_2$	30000	6.4×10^{17}	2.0	1:2	15–135	CsI/1.73	Öberg et al. (2007)
$H_2O:C^{18}O_2$	15000	1×10^{18}	2.0	2:1	15–135	CsI/1.73	Öberg et al. (2007)
$H_2O:C^{18}O_2$	4500	2.8×10^{17}	2.0	2:1	15–135	CsI/1.73	Öberg et al. (2007)
$H_2O:C^{18}O_2$	3750	1.3×10^{17}	2.0	4:1	15–135	CsI/1.73	Öberg et al. (2007)
$H_2O:C^{18}O_2$	15000	2.76×10^{18}	2.0	1:4	15–135	CsI/1.73	Öberg et al. (2007)
$H_2O:CO_2$	500	1.65×10^{18}	1.0	10:1	10–185	CsI/1.73	Ehrenfreund et al. (1999)
$H_2O:CO_2$	500	5.75×10^{17}	1.0	1:1	10–187	CsI/1.73	Ehrenfreund et al. (1999)
$CO_2:CH_3OH$	500	6×10^{17}	1.0	10:1	10–75	CsI/1.73	Ehrenfreund et al. (1999)
$CO_2:CH_3OH$	500	4.6×10^{17}	1.0	3:1	10–130	CsI/1.73	Ehrenfreund et al. (1999)
$CO_2:CH_3OH$	500	3.7×10^{17}	1.0	2:1	10–145	CsI/1.73	Ehrenfreund et al. (1999)
$CO_2:CH_3OH$	500	2.5×10^{17}	1.0	1:1	10–145	CsI/1.73	Ehrenfreund et al. (1999)
$CO_2:CH_3OH$	500	4.9×10^{17}	1.0	1:2	10–155	CsI/1.73	Ehrenfreund et al. (1999)
$CO_2:CH_3OH$	500	5.75×10^{17}	1.0	1:3	10–160	CsI/1.73	Ehrenfreund et al. (1999)
$CO_2:CH_3OH$	500	6.4×10^{17}	1.0	1:10	10–180	CsI/1.73	Ehrenfreund et al. (1999)
$CH_3OH:SO_2$	...	2.7×10^{17}	1.0	1:1	10	CsI/1.73	Boogert et al. (1997)
$CH_3OH:SO_2$	...	5×10^{17}	1.0	11:1	10	CsI/1.73	Boogert et al. (1997)
$CO:CO_2$	8000	1×10^{17}	0.5	1:1	15–100	...	Fraser & van Dishoeck (2004)
CO over HCOOH	16000	9.7×10^{16}	0.5	...	15–160	...	Fraser & van Dishoeck (2004)
CO under HCOOH	16000	9.7×10^{16}	0.5	...	15–160	...	Fraser & van Dishoeck (2004)

Table A.1. Continued.

Sample	Thickness (ML)	N_{ice} [a] (cm^{-2})	Resolution (cm^{-1})	Ratios	Temperature (K)/ UV radiation (time)	Substrate/ $n_{substrate}$	Reference
CO over CO_2	16000	3.1e17	0.5	...	15–160	...	Fraser & van Dishoeck (2004)
CO under CO_2	16000	4.3e17	0.5	...	15–100	...	Fraser & van Dishoeck (2004)
CO:HCOOH	8000	1.2e17	0.5	1:1	15–160	...	Fraser & van Dishoeck (2004)
CO under CH_3OH	16000	7.4e17	0.5	...	15–160	...	Fraser & van Dishoeck (2004)
CO over CH_3OH	16000	7.4e17	0.5	...	15–160	...	Fraser & van Dishoeck (2004)
CO over CH_4	8000	2.4e17	0.5	...	15–40	...	Fraser & van Dishoeck (2004)
CO under CH_4	8000	2.4e17	0.5	...	15–40	...	Fraser & van Dishoeck (2004)
CO over CO_2	1200	1e17	0.5	1:1	15–110	CsI/1.73	van Broekhuizen et al. (2006)
CO over CO_2	1800	1.6e17	0.5	1:2	15–110	CsI/1.73	van Broekhuizen et al. (2006)
CO_2 over CO	1200	9.8e16	0.5	1:1	15–110	CsI/1.73	van Broekhuizen et al. (2006)
CO_2 over CO	1800	3e17	0.5	2:1	15–110	CsI/1.73	van Broekhuizen et al. (2006)
CO_2 over CO	2400	1.9e17	0.5	3:1	15–110	CsI/1.73	van Broekhuizen et al. (2006)
CO_2 over CO	6600	6.7e17	0.5	10:1	15–110	CsI/1.73	van Broekhuizen et al. (2006)
$CO:CO_2$	1200	4.4e17	0.5	1:1	15–130	CsI/1.73	van Broekhuizen et al. (2006)
$CO:CO_2$	1800	1.9e17	0.5	2:1	15–130	CsI/1.73	van Broekhuizen et al. (2006)
$CO:CO_2$	6600	5.5e17	0.5	1:10	15–130	CsI/1.73	van Broekhuizen et al. (2006)
$H_2O:CH_3CHO$	2000	3.4e18	1.0	20:1	15–160	ZnSe/2.54	Terwisscha van Scheltinga et al. (2018)
$CO:CH_3CHO$	2000	3.1e18	1.0	20:1	15–160	ZnSe/2.54	Terwisscha van Scheltinga et al. (2018)
$CH_3OH:CH_3CHO$	2000	1.4e18	1.0	20:1	15–140	ZnSe/2.54	Terwisscha van Scheltinga et al. (2018)
$H_2O:CH_3CH_2OH$	2000	2.5e18	1.0	20:1	15–160	ZnSe/2.54	Terwisscha van Scheltinga et al. (2018)
$CO:CH_3CH_2OH$	2000	2.6e18	1.0	20:1	15, 30	ZnSe/2.54	Terwisscha van Scheltinga et al. (2018)
$CH_3OH:CH_3CH_2OH$	2000	4.6e18	1.0	20:1	15–150	ZnSe/2.54	Terwisscha van Scheltinga et al. (2018)
$H_2O:CH_3OCH_3$	2000	2.3e18	1.0	20:1	15–160	ZnSe/2.54	Terwisscha van Scheltinga et al. (2018)
$CO:CH_3OCH_3$	2000	2.7e18	1.0	20:1	15–120	ZnSe/2.54	Terwisscha van Scheltinga et al. (2018)
$CH_3OH:CH_3OCH_3$	2000	3.8e18	1.0	20:1	15–120	ZnSe/2.54	Terwisscha van Scheltinga et al. (2018)
$H_2O:CH_3COCH_3$	3500	2e18	0.5	5:1	15–160	ZnSe/2.54	Rachid et al. (2020)
$H_2O:CH_3COCH_3$	3500	2.6e18	0.5	20:1	15–160	ZnSe/2.54	Rachid et al. (2020)
$CO:CH_3COCH_3$	3500	1.9e18	0.5	5:1	15, 30	ZnSe/2.54	Rachid et al. (2020)
$CO:CH_3COCH_3$	3500	2e18	0.5	20:1	15, 30	ZnSe/2.54	Rachid et al. (2020)
$CO_2:CH_3COCH_3$	3500	1.3e18	0.5	5:1	15–100	ZnSe/2.54	Rachid et al. (2020)
$CO_2:CH_3COCH_3$	3500	1.4e18	0.5	20:1	15–100	ZnSe/2.54	Rachid et al. (2020)
$CH_3OH:CH_3COCH_3$	3500	2.6e18	0.5	5:1	15–140	ZnSe/2.54	Rachid et al. (2020)
$CH_3OH:CH_3COCH_3$	3500	5.5e18	0.5	20:1	15–140	ZnSe/2.54	Rachid et al. (2020)
$CH_3NH_2:H_2O$	3500	2.2e18	0.5	1:5	15–150	ZnSe/2.54	Rachid et al. (2021)
$CH_3NH_2:H_2O$	3500	2.5e18	0.5	1:10	15–150	ZnSe/2.54	Rachid et al. (2021)
$CH_3NH_2:H_2O$	3500	2.6e18	0.5	1:20	15–150	ZnSe/2.54	Rachid et al. (2021)
$CH_3NH_2:CH_4$	3500	1.9e18	0.5	1:5	15–45	ZnSe/2.54	Rachid et al. (2021)
$CH_3NH_2:CH_4$	3500	2e18	0.5	1:10	15–45	ZnSe/2.54	Rachid et al. (2021)
$CH_3NH_2:CH_4$	3500	2e18	0.5	1:20	15–45	ZnSe/2.54	Rachid et al. (2021)
$CH_3NH_2:NH_3$	3500	2.2e18	0.5	1:5	15–115	ZnSe/2.54	Rachid et al. (2021)
$CH_3NH_2:NH_3$	3500	2.4e18	0.5	1:10	15–115	ZnSe/2.54	Rachid et al. (2021)
$CH_3NH_2:NH_3$	3500	2.6e18	0.5	1:20	15–115	ZnSe/2.54	Rachid et al. (2021)
$CH_3OCHO:CO$	2000	1.8e18	0.5	1:20	15–120	ZnSe/2.54	Terwisscha van Scheltinga et al. (2021)

Table A.1. Continued.

Sample	Thickness (ML)	N_{ice}[a] (cm^{-2})	Resolution (cm^{-1})	Ratios	Temperature (K)/ UV radiation (time)	Substrate/ $n_{\text{substrate}}$	Reference
$CH_3OCHO:H_2CO$	2000	2.2e18	0.5	1:20	15–120	ZnSe/2.54	Terwisscha van Scheltinga et al. (2021)
$CH_3OCHO:CH_3OH$	2000	1.6e18	0.5	1:20	15–120	ZnSe/2.54	Terwisscha van Scheltinga et al. (2021)
$CH_3OCHO:H_2O$	2000	1.5e18	0.5	1:20	15–120	ZnSe/2.54	Terwisscha van Scheltinga et al. (2021)
$CH_3CN:H_2O$	5000	1.7e18	1.0	1:5	15–150	Ge/4.0	Rachid et al. (2022)
$CH_3CN:H_2O$	5000	2.3e18	1.0	1:10	15–150	Ge/4.0	Rachid et al. (2022)
$CH_3CN:H_2O$	5000	1.6e18	1.0	1:20	15–150	Ge/4.0	Rachid et al. (2022)
$CH_3CN:CO$	5000	1.3e18	1.0	1:5	15,30	Ge/4.0	Rachid et al. (2022)
$CH_3CN:CO$	5000	1.6e18	1.0	1:10	15,30	Ge/4.0	Rachid et al. (2022)
$CH_3CN:CO_2$	5000	1.2e18	1.0	1:5	15–150	Ge/4.0	Rachid et al. (2022)
$CH_3CN:CO_2$	5000	1.8e18	1.0	1:10	15–150	Ge/4.0	Rachid et al. (2022)
$CH_3CN:NH_3$	5000	2e18	1.0	1:5	15–150	Ge/4.0	Rachid et al. (2022)
$CH_3CN:NH_3$	5000	2.1e18	1.0	1:10	15–150	Ge/4.0	Rachid et al. (2022)
$CH_3CN:NH_3$	5000	2.1e18	1.0	1:20	15–150	Ge/4.0	Rachid et al. (2022)
Tertiary mixtures							
$HCOOH:H_2O:CO_2$	1800	1.5e18	1.0	0.1:1:0.4	15	CsI/1.73	Bisschop et al. (2007)
$HCOOH:H_2O:CH_3OH$	1800	1.6e18	1.0	0.1:1:0.4	15	CsI/1.73	Bisschop et al. (2007)
$HCOOH:H_2O:CO$	1800	1.74e18	1.0	0.1:1:0.4	15	CsI/1.73	Bisschop et al. (2007)
$H_2O:CO:O_2$	2500	3.8e17	1.0	1:80:20	10,30	CsI/1.73	Ehrenfreund et al. (1997)
$H_2O:CO:CO_2$	2500	3.3e17	1.0	1:50:50	10,30	CsI/1.73	Ehrenfreund et al. (1997)
$H_2O:CO:CO_2$	2500	3.7e18	1.0	1:50:56	10,45	CsI/1.73	Ehrenfreund et al. (1997)
$CO:O_2:CO_2$	2500	1.2e17	1.0	100:50:4	10,30	CsI/1.73	Ehrenfreund et al. (1997)
$CO:O_2:CO_2$	2500	1.2e17	1.0	100:50:8	10	CsI/1.73	Ehrenfreund et al. (1997)
$CO:O_2:CO_2$	2500	1.2e17	1.0	100:50:16	10,30	CsI/1.73	Ehrenfreund et al. (1997)
$CO:O_2:CO_2$	2500	1.2e17	1.0	100:50:21	10,30	CsI/1.73	Ehrenfreund et al. (1997)
$CO:O_2:CO_2$	2500	1.2e17	1.0	100:50:32	10	CsI/1.73	Ehrenfreund et al. (1997)
$CO:O_2:CO_2$	2500	1.2e17	1.0	100:54:10	10,30	CsI/1.73	Ehrenfreund et al. (1997)
$CO:O_2:CO_2$	2500	1.2e17	1.0	100:20:11	10,30	CsI/1.73	Ehrenfreund et al. (1997)
$CO:O_2:CO_2$	2500	1.2e17	1.0	100:11:20	10,30	CsI/1.73	Ehrenfreund et al. (1997)
$CO:O_2:CO_2$	2500	1.2e17	1.0	100:10:23	10,30	CsI/1.73	Ehrenfreund et al. (1997)
$H_2O:CO:N_2$	2500	2e17	1.0	1:40:50	10,30	CsI/1.73	Ehrenfreund et al. (1997)
$CO:N_2:CO_2$	2500	1.2e17	1.0	100:50:20	10,30	CsI/1.73	Ehrenfreund et al. (1997)
$H_2O:CO_2:CO$	2500	2.7e17	1.0	100:20:3	20	CsI/1.73	Ehrenfreund et al. (1997)
$H_2O:CH_3OH:CO_2$	500	1.2e18	1.0	9:1:2	10–185	CsI/1.73	Ehrenfreund et al. (1999)
$H_2O:CH_3OH:CO_2$	500	2.8e17	1.0	0.2:0.6:1	10–140	CsI/1.73	Ehrenfreund et al. (1999)
$H_2O:CH_3OH:CO_2$	500	2.8e17	1.0	0.4:0.6:1	10–140	CsI/1.73	Ehrenfreund et al. (1999)
$H_2O:CH_3OH:CO_2$	500	6e17	1.0	1:0.6:1	10–180	CsI/1.73	Ehrenfreund et al. (1999)
$H_2O:CH_3OH:CO_2$	500	9.8e17	1.0	0.7:0.7:1	10–146	CsI/1.73	Ehrenfreund et al. (1999)
$H_2O:CH_3OH:CO_2$	500	1.5e18	1.0	0.8:0.9:1	10–135	CsI/1.73	Ehrenfreund et al. (1999)
$H_2O:CH_3OH:CO_2$	500	2.7e18	1.0	1:1:1	10–145	CsI/1.73	Ehrenfreund et al. (1999)
$H_2O:CH_3OH:CO_2$	500	4.9e17	1.0	0.7:1:1	10–120	CsI/1.73	Ehrenfreund et al. (1999)
$H_2O:CH_3OH:CO_2$	500	1.8e16	1.0	0.6:1:0.8	10–121	CsI/1.73	Ehrenfreund et al. (1999)
$H_2O:CH_3OH:CO_2$	500	7.8e17	1.0	1.2:0.7:1.0	10–119	CsI/1.73	Ehrenfreund et al. (1999)
$H_2O:CH_3OH:CO_2$	500	3e17	1.0	0.7:0.9:1.0	10–134	CsI/1.73	Ehrenfreund et al. (1999)
$H_2O:CH_3OH:CO_2$	500	5e16	1.0	0.5:1:1	10	CsI/1.73	Ehrenfreund et al. (1999)
$H_2O:CH_3OH:CO_2$	500	9.7e16	1.0	0.9:1.4:1	10–125	CsI/1.73	Ehrenfreund et al. (1999)

Table A.1. Continued.

Sample	Thickness (ML)	N_{ice} [a] (cm^{-2})	Resolution (cm^{-1})	Ratios	Temperature (K)/ UV radiation (time)	Substrate/ $n_{substrate}$	Reference
H_2O:CH_3OH:CO_2	500	7.9e16	1.0	0.2:0.5:1	10, 98	CsI/1.73	Ehrenfreund et al. (1999)
H_2O:CH_3OH:CO_2	500	7.7e16	1.0	0.3:0.5:1	10–95	CsI/1.73	Ehrenfreund et al. (1999)
H_2O:CH_3OH:CO_2	500	7.1e16	1.0	0.3:0.7:1	10–82	CsI/1.73	Ehrenfreund et al. (1999)
H_2O:CH_3OH:CO_2	500	1.2e18	1.0	1.1:1.2:1	10–131	CsI/1.73	Ehrenfreund et al. (1999)
H_2O:CH_3OH:CO_2	500	3e17	1.0	0.7:0.9:1	10–134	CsI/1.73	Ehrenfreund et al. (1999)
H_2O:CH_3OH:CO_2	500	7.2e17	1.0	0.9:0.3:1	10–115	CsI/1.73	Ehrenfreund et al. (1999)
CO:CH_3OH:CH_3CHO	2000	1.8e18	1.0	20:20:1	15–120	ZnSe/2.54	Terwisscha van Scheltinga et al. (2018)
CO:CH_3OH:CH_3CH_2OH	2000	1.8e18	1.0	20:20:1	15–150	ZnSe/2.54	Terwisscha van Scheltinga et al. (2018)
CO:CH_3OH:CH_3OCH_3	2000	1.7e18	1.0	20:20:1	15–100	ZnSe/2.54	Terwisscha van Scheltinga et al. (2018)
CH_3COCH_3:H_2O:CO_2	3500	7.2e17	0.5	1:2.5:2.5	15–160	ZnSe/2.54	Rachid et al. (2020)
CH_3COCH_3:H_2O:CO_2	3500	6.8e17	0.5	1:10:10	15–160	ZnSe/2.54	Rachid et al. (2020)
CH_3COCH_3:CO:CH_3OH	3500	9.7e17	0.5	1:2.5:2.5	15–140	ZnSe/2.54	Rachid et al. (2020)
CH_3COCH_3:CO:CH_3OH	3500	1e18	0.5	1:10:10	15–140	ZnSe/2.54	Rachid et al. (2020)
CH_3NH_2:H_2O:CH_4	2500	1.1e18	0.5	1:5:5	15–150	ZnSe/2.54	Rachid et al. (2021)
CH_3NH_2:H_2O:CH_4	2500	1.2e18	0.5	1:10:10	15–150	ZnSe/2.54	Rachid et al. (2021)
CH_3NH_2:H_2O:NH_3	2500	1.2e18	0.5	1:5:5	15–150	ZnSe/2.54	Rachid et al. (2021)
CH_3NH_2:H_2O:NH_3	2500	1.3e18	0.5	1:10:10	15–150	ZnSe/2.54	Rachid et al. (2021)
CH_3NH_2:CH_4:NH_3	2500	1.1e18	0.5	1:5:5	15–115	ZnSe/2.54	Rachid et al. (2021)
CH_3NH_2:CH_4:NH_3	2500	1.2e18	0.5	1:10:10	15–115	ZnSe/2.54	Rachid et al. (2021)
CH_3CN:H_2O:CO_2	5000	1.3e18	1.0	1:5:2	15–150	Ge/4.0	Rachid et al. (2022)

Quaternary mixtures

Sample	Thickness (ML)	N_{ice} [a] (cm^{-2})	Resolution (cm^{-1})	Ratios	Temperature (K)/ UV radiation (time)	Substrate/ $n_{substrate}$	Reference
H_2O:CO:O_2:N_2	2500	2.6e17	1.0	1:40:40:15	10,30	CsI/1.73	Ehrenfreund et al. (1997)
H_2O:CH_3OH:CO_2:NH_3	500	3.1e17	1.0	0.7:0.7:1:0.7	10–104	CsI/1.73	Ehrenfreund et al. (1999)
H_2O:CH_3OH:CO_2:CH_4	500	3.1e17	1.0	0.6:0.7:1:0.1	10–119	CsI/1.73	Ehrenfreund et al. (1999)
H_2O:CH_3OH:CO_2:CH_4	500	1e17	1.0	0.4:0.6:1:0.23	10	CsI/1.73	Ehrenfreund et al. (1999)
CO:O_2:N_2:CO_2	2500	4.4e18	1.0	1:50:25:32	10,30	CsI/1.73	Ehrenfreund et al. (1997)
CH_3OCHO:CO:H_2CO:CH_3OH	2000	8.9e17	0.5	1:20:20:20	15–120	ZnSe/2.54	Terwisscha van Scheltinga et al. (2021)
CH_3NH_2:H_2O:CH_4:NH_3	3400	9.3e17	0.5	3:10:10:10	15–120	ZnSe/2.54	Rachid et al. (2021)
CH_3CN:H_2O:CH_4:NH_3	5000	2.3e18	1.0	1:20:2:2	15–150	Ge/4.0	Rachid et al. (2022)

Five components mixture

Sample	Thickness (ML)	N_{ice} [a] (cm^{-2})	Resolution (cm^{-1})	Ratios	Temperature (K)/ UV radiation (time)	Substrate/ $n_{substrate}$	Reference
H_2O:CO:O_2:N_2:CO_2	2500	3.8e17	1.0	1:50:35:15:3	10	CsI/1.73	Ehrenfreund et al. (1997)
H_2O:CO:O_2:N_2:CO_2	500	8e16	1.0	1:50:35:15:3	10	CsI/1.73	Ehrenfreund et al. (1997)

Notes. [a] Except in the case of pure ices, N_{ice} values correspond to the major ice component.

Table B.1. Example of relational database for pure H_2O ice. All information is visible in the user interface.

ID[a]	Name[b]	Deposition temperature (K)	Author	DOI	Upload date	Annotation[b]
			Analogue			
14	Pure H_2O 3000 ML	15	Öberg et al.	10.1051/0004-6361:20065881	2021-10-27	Pure_H2O_3000_ML.csv
ID[a]	Temperature (K)	Column density (molec./cm^2)	Ice thickness (μm)	Resolution (cm^{-1})	Wavenumber range (cm^{-1})	File name[c]
			Spectrum			
14	15	1e17	3000	2.0	500–4000	96_15.0K

Notes. [a] identifier number that relates the analog to the spectrum.
[b] Annotation file containing the respective positions and assignments of the vibration modes.
[c] Name of the file containing the wave number and absorbance of the ice sample when uploaded to the database. This file is stored in HDF5 format in LIDA and available for download as an `ascii` file.

Appendix B: Database design and back-end information

The structure of LIDA is built with `Flask`[27] (Grinberg 2018), an open-source web framework written in Python. `Flask` is widely extensible in the sense that external software can be embedded in the web application. LIDA has two major interfaces that provide access to administrators and users, respectively. The user interface is described in Section 3.1. Here, we provide details of the administrator interface, which is obviously only accessible via an account and is thus restricted to collaborators and developers.

The administrator interface provides access to all information hosted in the database, as well as the capability to add and modify data. In this module, the database is structured in a relation design between **analogs** and **spectra**. *Analogues* are ice sample (e.g., Pure H_2O), whereas *a spectrum* is the IR spectrum of the analog at a specific temperature (e.g., Pure H_2O at 15 K). Table B.1 shows a scheme of the information contained in the database. All this information is also visible in the user interface, which is introduced in Section 3.1.

In addition to the IR spectra of ice samples, the database hosts data of experimentally derived UV/vis refractive index values (optical constants) and calculated values for the mid-IR. The continuum SED of protostars is also hosted, but it is only accessible via the online tool SPECFY. The database files containing this information, are also structured in a relational design as used for *analogs* and *spectra*. The files containing the spectral data, optical constants, and continuum SED are stored on the server using a hierarchical data format (HDF5) that has been designed to store a large amount of data. The web interface allows the administrator to upload the data as a simple two-column file. The first column (X-axis) is the wave number (cm^{-1}) for the absorbance and refractive index data, whereas wavelength (μm) is used for continuum SED data. Likewise, the second column (Y-axis) gives the physical quantities such as absorbance, refractive index, and flux in Jy, respectively. Python has a package supporting HDF5 called H5PY[28], which is used to generate compressed files in LIDA to improve the efficiency of the database. Despite the files being stored in HDF5 format, they are available for download by the user as ASCII files (`.txt` extension). For security reasons, LIDA performs a check when uploading data that consists of validating the file extension, structure, and size. Absorbance data can be uploaded under the category of warm-up or irradiation time (exposition). Similarly, the refractive index is uploaded under the category of real or imaginary values. The continuum SED data is uploaded in the polynomial or blackbody categories.

The administrator module also contains the *"access information tracker",* which makes it possible to track the number of accesses and downloads over the months and years. The goal of this feature is to check the impact of LIDA in providing the astronomical community with essential and accurate data to interpret telescope observations.

Appendix C: Web interfaces of the online tools

The web interface of SPECFY is shown in Figure C.1. In "Step 1", SPECFY sets the wavelength range to create the synthetic spectrum. This step is crucial because some absorbance spectra in the database have different ranges. By setting the range, all the absorbance spectra selected in step 2 are evenly interpolated to ensure that all spectral components have the same range. Next, in "Step 2", the laboratory ice spectrum from LIDA can be selected to be converted to an optical depth scale and combined to another ice spectrum. This step can be repeated multiple times. Finally, in "Step 3", the optical depth scale spectrum is converted to a spectrum in flux units based on the object and the continuum SED model adopted by the user. An example of the output files is shown in Figure C.2. The *top* panel shows the combined spectrum used to match the AFGL 989 *ISO* spectrum. The *bottom* panel displays the synthetic spectrum in flux scale that adopts the continuum SED of the Elias 29 protostar.

Figure C.3 shows the web interface of the refractive index calculator. This tool requires the upload of an external file containing the absorbance spectrum, which is done via the "Submit' button'. Next, the user is asked to parse the values of three physical parameters (ice thickness, $n_{670\,nm}$, n_{subs}) and the stop criteria (MAPE). The calculations can be started by clicking on the blue button labeled "Start calculation", and they roughly last 1–4 seconds for a spectrum with 18000 rows. The output data can be download by clicking on the green button labeled "Download the refractive index". One of the outputs is called "`lnk_optool`". This file contains

---

[27] https://flask.palletsprojects.com/en/2.0.x/
[28] https://docs.h5py.org/en/stable/

Tool for creating protostellar synthetic spectrum containing ice features

This tool allows to combine different ice spectra from this datatabase to produce a synthetic infrared spectrum in optical depth scale. A linear combination of the laboratory spectrum is used. Additionally, the spectrum can be used to create a protostellar spectrum by adopting a continuum template.

Step 1: Set the spectral range

Wavelength 1:   **Wavelength 2:**

[Set ranges]

Step 2: Select the spectrum for the linear combination and provide the required column density.
You can successively add ice spectrum at this step.

Analogue: **Temperature:**

[Pure HCOOH   ⌄]   [⌄]

Column density (molec. cm^{-2}):

[   ]

[Add spectrum]

Step 3: Select the continuum template.

Object: **Continuum model:**

[Select continuum   ⌄]   [⌄]

[Add continuum]

[Download the continuum SED files!]

Fig. C.1. Screenshot of web interface of SPECFY showing the three steps to create a synthetic protostar spectrum. The green buttons submit the information added to the white rectangles. In steps 2 and 3, the user can scroll and search for ice analogs and temperatures, and for continuum models, respectively. The blue button allows the user to download the continuum SED files.

the real and imaginary parts of the refractive index that are formatted to be used as input in the computational code `optool`[29] (Dominik et al. 2021), a command-line tool written in `Fortran`, which is dedicated to deriving the opacity of ice and bare grains.

---

[29] https://github.com/cdominik/optool
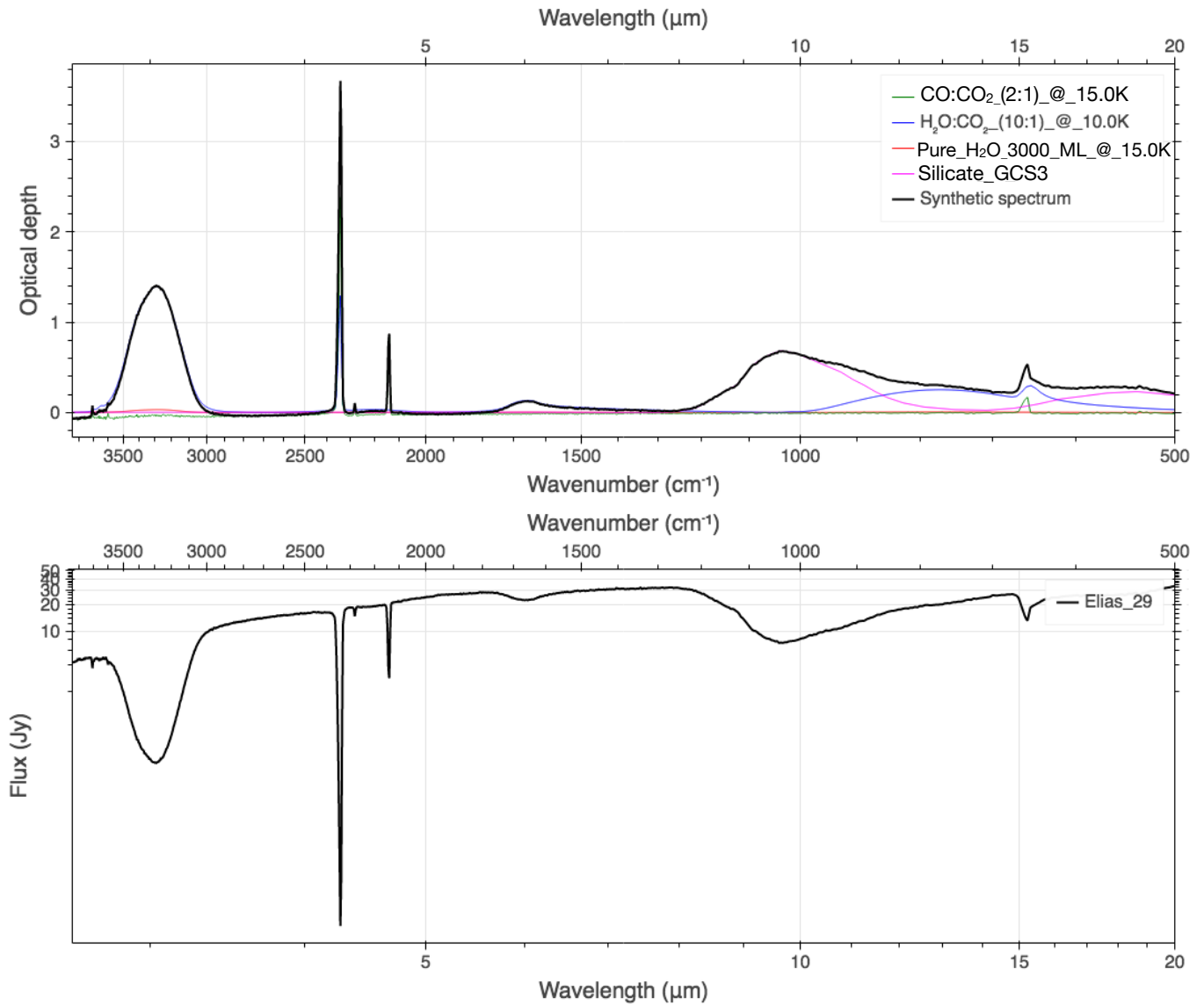
Fig. C.2. Screenshot of outputs of the SPECFY online tool. Top: Synthetic spectrum in optical depth scale composed by the linear combination of three ice spectra (Pure H_2O, H_2O:CO_2, CO:CO_2) and silicate template from GCS 3 source. Bottom: Synthetic spectrum in flux scale adopting the Elias 29 protostar continuum SED, taken from Boogert et al. (2008).

Tool for calculating IR complex refractive index

This tool uses the source code from NKABS Python package for calculating the complex refractive index of astrophysical ices from the absorbance spectrum. The methodology adopted in this code is detailed in Rocha & Pilling (2014). The input parameters are the absorbance spectrum with the wavenumber (cm^{-1}) the thickness of the ice (d), the refractive index of the ice at 670 nm (n$_0$), the refractive index of the substrate (n$_2$) and the Mean Average Percentual Error (MAPE) as the stop criteria. The outputs of the code are the real (n) and imaginary (k) part of the refractive index with the wavelength.

Fig. C.3. Screenshot of web interface of the online tool for calculating the refractive index of ices. The user can upload the absorbance spectrum as input data and provide the ice parameters. The calculations are started by clicking on the blue button labeled "Start calculation", and the files with the results are downloaded by clicking on the green button labeled "Download the refractive index". The bottom yellow box informs that other formats of this tool are available for download as well.